The 2015/2016 El Niño Event in Context of the MERRA-2 Reanalysis: A Comparison of the Tropical Pacific with 1982/1983 and 1997/1998

Young-Kwon Lim[1,2], Robin M. Kovach[1,3], Steven Pawson [1], and Guillaume Vernieres[1,3]

[1]Global Modeling and Assimilation Office, NASA GSFC, Greenbelt, MD

[2]Goddard Earth Sciences Technology and Research, I. M. Systems Group, Greenbelt, MD

[3]Space Science Applications International, Lanham, MD

Corresponding Author: Young-Kwon Lim

(Young-Kwon.Lim@nasa.gov, 1-301-614-6906)

For Submission of the Revised Version to Journal of Climate

February 17, 2017

Abstract

The 2015/2016 El Niño is analyzed using atmospheric/oceanic analysis produced using the Goddard Earth Observing System (GEOS) data assimilation systems. As well as describing the structure of the event, a theme of the work is to compare and contrast it with two other strong El Niños, in 1982/1983 and 1997/1998. These three El Niño events are included in the Modern-Era Retrospective analysis for Research and Applications (MERRA) and in the more recent MERRA–2 reanalyses. MERRA-2 allows a comparison of fields derived from the underlying GEOS model, facilitating a more detailed comparison of physical forcing mechanisms in the El Niño events.

Various atmospheric/oceanic structures indicate that the 2015/2016 El Niño maximized in the Niño3.4 region, with the large region of warming over most of the Pacific and Indian Ocean. The eastern tropical Indian Ocean, Maritime Continent, and western tropical Pacific are found to be less dry in boreal winter, compared to the earlier two strong events.

While the 2015/2016 El Niño had an earlier occurrence of the equatorial Pacific warming and was the strongest event on record in the central Pacific, the 1997/1998 event exhibited a more rapid growth due to stronger westerly wind bursts and Madden-Julian Oscillation during spring, making it the strongest El Niño in the eastern Pacific. Compared to 1982/1983 and 1997/1998, the 2015/2016 event has a shallower thermocline over the eastern Pacific with a weaker zonal contrast of sub-surface water temperatures along the equatorial Pacific. While the three major ENSO events have similarities, each are unique when looking at the atmosphere and ocean surface and sub-surface.

1. Introduction

This study presents an analysis of the atmospheric and oceanic signals over the tropics associated with the strong El Niño event that occurred in 2015/2016. For the ocean, the study uses the Goddard Earth Observing System (GEOS) oceanic analysis (Vernières et al. 2012) that is driven by the Modern-Era Retrospective analysis for Research and Applications (MERRA) atmospheric reanalysis (Rienecker et al. 2011). Atmospheric fields in this work are from the updated MERRA-2 reanalysis (Bosilovich et al. 2015; Gelaro et al. 2016). These reanalysis datasets, described in more detail in Section 2, facilitate a quantitative examination of the large-scale climate anomalies associated with the 2015/2016 El Niño, in the context of a data record that includes more than 35 years of global analyses based on satellite and in-situ observations.

Numerous indices show that the 2015/2016 El Niño event is one of the three strongest events in the last 66 years (1950/1951–2015/2016) (Bell et al. 2016; Huang et al. 2016). The two other strongest events occurred in 1982/1983 and 1997/1998. Sea surface temperature (SST) anomalies for the established ENSO indicator regions show that while the 2015/2016 El Niño showed the largest anomalies over the Niño3.4 region (in late 2015) that partly covers the central Pacific (CP), it was substantially weaker than the 1997/1998 El Niño in the eastern Pacific (EP) (L´Heureux et al. 2016). However, regarding ranking the strongest ENSO events while incorporating the Niño 3.4 SST data uncertainty, Huang et al. (2016) pointed out that the strength of the three strongest events is not clearly separable at the 95% confidence level.

The Multivariate El Niño Southern Oscillation Index (MEI) (Wolter and Timlin 1998) that combines analysis of multiple meteorological and oceanographic components indicates that 1997/1998 is the strongest El Niño event during El Niño developing stage (i.e., 1982, 1997, and 2015). Our analysis of the atmospheric and oceanic structures also reveals that the 2015/2016 El

Niño is the strongest around the Niño3.4 region (e.g., Figs. 2, 4, 6, and 7), but that the 1997/1998 is the overall strongest event when assessed by conditions over the EP, the westerly wind burst (WWB) (McPhaden et al. 1988; Kerr 1999; McGregor et al. 2015), sub-surface water temperature, and anomalies in the thermocline depth.

Another aspect of interest about the 2015/2016 event is the relationship between the early onset of the 2015/2016 event and the oceanic state in 2014. The time evolution of the sea surface temperature (SST) anomaly in 2015 reveals an earlier appearance (January) of weak warm conditions over the central to eastern tropical Pacific than in the other two years. It is suggested that this early detection of the El Niño-like signal in January 2015 is associated with the positive SST anomaly, which is a remnant (or re-emergence) of the weak warming over the equatorial Pacific that occurred in 2014 (McPhaden 2015; L´Heureux et al. 2016). A strong El Niño was forecasted for 2014/2015 boreal winter because of the strong WWB and substantial buildup of warm water volume over the equatorial Pacific in early 2014 (McGregor et al. 2015; McPhaden 2015). However, this El Niño did not develop as expected, primarily due to an unexpected occurrence of a large easterly wind burst that hindered further growth of El Niño in summer (Min et al. 2015; Levine and McPhaden 2016). The 2014 forecast has thus been described as a "busted" forecast (Larson and Kirtman 2015). In contrast with the situation in 2014, the WWBs continued throughout 2015 and a strong warm ENSO reached maturity in the 2015/2016 boreal winter.

Although the three El Niño events (1982/1983, 1997/1998, and 2015/2016) are considered similar in view of their predominant strength, the basic characteristics in their oceanic and atmospheric structures are understood to be different from one another (Bell et al. 2016; L´Heureux et al. 2016), and further detailed investigations are still necessary. Specifically,

oceanic background in the El Niño onset period, the El Niño growth mechanism, and the type of the El Niño and the corresponding atmospheric structures in 2015 are quite different from those in the other two events (see Sections 3 and 4). Detailed comparisons of the three strongest El Niño events in both oceanic and atmospheric perspective are expected to provide very useful insight into their similarities and differences. We also expect that this comparison study will promote overall understanding of the latest strong El Niño event (2015/2016).

Another motivation of this study is to deliver the current status of the MERRA-2 atmospheric data and the MERRA-driven GEOS ocean analysis in reproducing characteristics of the historically strong El Niño events. Some of the oceanic structures presented in this study are generally consistent with those in L´Heureux et al. (2016). We compared several atmospheric and oceanic structures shown in our study with those produced from the observations of SST, cloud and precipitation, and the Interim Re-Analysis of the European Center for Medium-Range Weather Forecasts (ERA-Interim; Dee et al. 2011) to demonstrate the capability of the GEOS data assimilation system and robustness of our conclusions.

Having characterized the El Niño events including their intercomparison in Section 3, a closer examination of transience is presented in Section 4. A particular focus is on exploring the time evolution of SST, sub-surface ocean water, WWBs, and the Madden-Julian Oscillation (MJO) activity (Kessler et al. 1995; Yu and Rienecker 1998). These factors are examined in the context of their role in determining the growth and strength of the El Niño events.

2. Data

The present study will perform this investigation utilizing the Modern-Era Retrospective analysis for Research and Applications version 2 (MERRA-2) (Gelaro et al. 2016), the new

115 global reanalysis dataset developed by NASA Goddard Space Flight Center (GSFC) / Global
116 Modeling and Assimilation Office (GMAO). The MERRA-2 atmospheric general circulation
117 model (AGCM) was computed on the cubed sphere grid (Putman and Lin 2007) to allow
118 relatively uniform grid spacing at all latitudes. Compared to the previous version, MERRA,
119 numerous upgrades were made to the model's physical parameterizations including moist
120 process (e.g., increased re-evaporation of frozen precipitation and cloud condensate, resolution-
121 aware parameters, and Tokioka-type trigger on deep convection as part of the Relaxed Arakawa-
122 Schubert (RAS, Moorthi and Suarez 1992) convective scheme), turbulence, land and ocean
123 surface, and gravity wave drag. In addition, the assimilation of interactive aerosols was
124 implemented into the system, a feature of the Earth system absent from previous reanalyses
125 (Bosilovich et al. 2015). Further details of the upgrades made to the MERRA-2 system are
126 described in Bosilovich et al. (2015), Molod et al. (2015), and Gelaro et al. (2016).

127 The key atmospheric variables used for this study consist of the 2-meter air temperature
128 (2mT), precipitation, sea level pressure, wind stress, 10-meter level wind, tropospheric winds,
129 temperatures, specific humidities, and total cloud fractions (GMAO 2015a,b,c,d,e,f,g) at each
130 vertical pressure level up to the tropopause. Horizontal resolution of the MERRA-2 data is a
131 0.625°×0.5° longitude/latitude grid. We additionally take advantage of the ERA-Interim (Dee et
132 al. 2011) to demonstrate the robustness of our conclusions by comparing several major spatial
133 patterns (e.g., temperature and precipitation anomalies) calculated from each reanalysis data set.

134 As a validation of the MERRA-2 cloud and precipitation, we compare them with the
135 satellite-based observations obtained from the International Satellite Cloud Climatology Project
136 (ISCCP) (Schiffer and Rossow 1983) and Moderate-resolution Imaging Spectroradiometer
137 (MODIS) (Guenther et al. 1996) for cloud fraction, and from the Tropical Rainfall Measuring

Mission (TRMM) and Integrated Multi-satellite Retrievals for GPM (IMERG) (Huffman et al. 2007, 2015) for precipitation. As the TRMM satellite mission was terminated in 2015, the transition from the TRMM data products to the Global Precipitation Measurement (GPM) mission products has begun to produce GPM-era IMERG data sets. We use IMERG precipitation data for 2015/2016 and TRMM data for the 1997/1998 El Niño.

SST data are obtained from both the Hadley Centre Global SST (HadISST) (Rayner et al. 2003) and Reynolds Optimal Interpolation Sea Surface Temperature (OISST) (Reynolds et al. 2007). Sub-surface temperatures over the equatorial Pacific are also analyzed to compare their anomalous structures between the three strongest El Niño events. We obtained the sub-surface temperature, ocean surface current, and sea surface salinity (SSS) estimates from the ocean and sea-ice retrospective analysis MERRA-Ocean (Keppenne et al., 2008; Vernieres et al., 2012). The weakly coupled MERRA-Ocean reanalysis consists of an ocean analysis conducted during a coupled model integration, with the atmospheric state of the atmosphere-ocean coupled general circulation model (AOGCM) constrained to MERRA up until December 2015 and MERRA-2 from January 2016 onward. The ocean data assimilation system assimilates gridded SST retrievals, Argo (Gould et al. 2004) temperature and salinity profiles, temperature/salinity profiles from eXpendable BathyThermographs (XBTs) and Conductivity Temperature Depths (CTDs) (http://www.aoml.noaa.gov/phod/dhos/xbt_ctd.php), and temperature observations from the tropical moorings. The sea-ice assimilation is tightly coupled with the ocean analysis, in that the temperature and salinity of the upper ocean are corrected to be consistent with the assimilated sea-ice concentration from National Snow and Ice Data Center (NSIDC) (Maslanik and Stroeve 1999). Ice thickness is modified by subsequent integration of the coupled ocean-sea-ice model.

A critical issue of ocean reanalysis is the lack of salinity observations prior to the advent of

Argo. This problem is illustrated in Fig. 1 which depicts the evolution of the tropical salinity *in-situ* observing system during the month of December for 1982 (top), 1997 (middle) and 2015 (bottom). It is clear that prior to the full array of Argo floats in 2006, MERRA-Ocean's estimate of SSS is mostly driven by the climatological relaxation imposed on surface salinity as well as the model derived surface fresh water fluxes. This caveat in the salinity observing system is the cause of the large SSS differences seen between 2015 and 1997 as well as 2015 and 1982 in the two upper panels of Fig. 6.

3. Morphology of the 2015/2016 El Niño Event

3.1 Ocean Temperatures

Figure 2 shows time series of the SST anomalies for the established indicator regions. SST in the Niño3.4 and Niño 4 regions, where the CP (defined here as 160°E–150°W) is partially (Niño 3.4 (5°N–5°S, 170°–120°W)) and purely (Niño 4 (5°N–5°S, 160°E–150°W)) included, for the mature El Niño stage of September 2015 – February 2016 were 2.6°C and 1.4°C, respectively. These can be compared to values of 2.5°C and 0.7°C in the 1997/1998 event. In contrast, the SST anomalies over the Niño 3 and Niño 1+2 region (representing the eastern tropical Pacific) were 2.6°C and 1.9°C, which are smaller than the corresponding values of 3.2°C and 3.8°C in the 1997/1998 event. These differences in the SST anomaly indices highlight the importance of considering the spatial structure when quantifying the strength of the El Niño event. Please note that, although the 2015/2016 event has the maximum Niño 3.4 SST based on the Reynolds OISST and MERRA-Ocean data, comparison in the El Niño strength based on the Niño 3.4 SST needs caution because of some uncertainties in various SST products (Huang et al. 2016).

184 Figure 3 and the left panel in Fig. 4 show the spatial distribution of SSTs and their
185 differences over the tropical Pacific for December 1982, 1997 and 2015. It is evident from both
186 figures that the 2015 ENSO event was much warmer than both the 1982 and 1997 event in the
187 central to western Pacific (WP) and much colder in the far EP (south of equator). The El Niño
188 Modoki index that defines the type of El Niño from SST anomalies over the tropical Pacific
189 (Ashok et al. 2009: http://www.jamstec/frcgc/research/d1/iod/DATA/emi.monthly.txt) supports
190 the relation to the CP warming in 2015/2016. However, Niño indices in Fig. 2 reveal that SST in
191 Niño 4 is not greater than the SST in Niño 3 (Kug et al. 2009; Yeh et al. 2009), indicating that
192 2015/2016 is not a complete CP-type El Niño. Comparison between 1982 and 1997 in Figure 4c
193 indicates that the El Niño in 1997 was stronger than in 1982 in terms of SST warming over the
194 eastern tropical Pacific at El Niño maturity.
195 Ocean current anomalies produced by the GEOS Ocean Data Assimilation System
196 (ODAS) are examined for the boreal winter period of three El Niño events. Difference fields in
197 Figs. 4d-f show that the westerly current anomaly is relatively weaker in 2015/2016 along the
198 equatorial Pacific, compared to the earlier two super El Niño events (Figs. 4d,e). Details on the
199 near-surface zonal wind anomaly as a forcing to trigger the westerly ocean current anomaly and
200 grow El Niño will be further discussed in Section 4.2.
201 Sub-surface ocean temperatures along the equator in December for the three events are
202 shown in Fig. 5. The relative locations of the temperature maxima vary among the years, with
203 the highest temperatures to the west of the dateline in 2015 but to the east of it in 1982 and 1997.
204 In normal conditions, the trade winds along the equator blow to the west, piling up warm surface
205 water off of Asia, and depressing the thermocline in the WP. In a typical El Niño, these trade
206 winds relax, leading to a flattening of the thermocline (rising in the west and deepening in the

207 east). This deepening of the thermocline in the east suppresses the upwelling of cool water,
208 developing the condition that the SST and subsurface water in the EP can be warmer than
209 normal. This is the case for the El Niño events of 1982/1983 and 1997/1998. However, in
210 2015/2016, the thermocline is not flat but shallower in the east (see 20°C isotherm in the EP), so
211 the water temperature increase over the far EP is less dominant. The WP warm pool displaced
212 eastward by zonal advection (through westerly trade wind anomaly) (Wang and McPhaden 2000)
213 appears to remain more in the CP, rather than in the EP.

214 SSS is generally fresher over the tropical ocean where there is more precipitation than
215 evaporation. The shading in Fig. 6 represents difference fields in SSS between the three El Niño
216 winters (DJF). It is clear that the SSS driven from the MERRA ocean data assimilation system is
217 fresher over the CP around the dateline in the 2015/2016 El Niño than in the other two super El
218 Niño events (Figs. 6a,b). Figure 6 shows that the precipitation minus evaporation (PME)
219 (depicted by contours) from MERRA-2 is also maximized near the CP in the 2015/2016 El Niño.
220 Also, north of the equator over the eastern tropical Pacific shows fresher SSS values for
221 2015/2016. This is in good agreement with previous studies that the precipitation band associated
222 with the EP Intertropical convergence zone (ITCZ) during El Niño, when the maximum SST
223 anomalies span both the CP and EP, is relatively north of the precipitation band for the EP El
224 Niño event (see Fig. 8) (Kao and Yu 2009; Weng et al. 2009; Xie and Yang 2014). Difference in
225 SSS between 1997/1998 and 1982/1983 (Fig. 6c) suggests more PME and fresher SSS over the
226 far EP in 1997/1998 (see Fig. 7 and area-averaged precipitation in Table 1). Overall, Fig. 6
227 explains that the SSS difference field driven from the GEOS ODAS system matches the PME
228 difference field quite well over the tropical ocean. One thing to note is that the SSS difference
229 fields in the two upper panels that include 2015/2016 (Figs. 6a,b) contain the effect of the

salinity observing system upgrade, as it was explained in Section 2 and Fig. 1, resulting in larger magnitude of SSS difference in general, compared to Fig. 6c.

Taken together, these oceanic features highlight the fact that the 2015/2016 event was stronger in the CP due to the fact that the maximum SST anomalies are shifted west of those in the other two events. The other two large events were less pronounced in the CP, but had a bigger impact in the EP – where the 1997/1998 event is the strongest in the record.

3.2 Atmospheric Structure

El Niño is known to drive wet conditions over the central to eastern tropical Pacific, and dry conditions over the Maritime Continent, WP, and eastern side of South America (e.g., Amazonia) along the tropical region. Figure 7 shows the precipitation anomalies for each El Niño event. The distribution in the sign of precipitation anomalies tends to be close between all three El Niño periods. Some noticeable differences between the three El Niño periods are that 1) the magnitude of the positive anomaly over the eastern tropical Pacific is largest in the 1997/1998 El Niño, 2) the location of the maximum positive anomaly over the tropics in 2015/2016 is relatively west of the locations for 1982/1983 and 1997/1998, and 3) drought over the eastern tropical Indian Ocean is weaker in 2015/2016. These features are again clarified in Table 1 that compares the strength of El Niño in different tropical regions in terms of 2mT and precipitation anomalies.

In order to confirm that MERRA-2 precipitation and total cloud examined in this study are realistic, they were compared with satellite-based observations. Figure 8 compares the precipitation between 1997/1998 and 2015/2016 El Niño events using the MERRA-2 reanalysis (Fig. 8a) and TRMM / IMERG observations (Fig. 8b), respectively. It is clear that MERRA-2 reproduces the observational difference in precipitation between the two El Niño events quite

well. Increased precipitation north of the equator in 2015 is associated with the location of the EP ITCZ north of that for EP El Niño (Kau and Yu 2009; Weng et al. 2009; Xie and Yang 2014).

The MERRA-2 cloud product is validated using ISCCP and MODIS observations (Fig. 9). Figure 9 clearly demonstrates that distribution of the total cloud fraction anomalies retrieved from ISCCP (1997/1998 El Niño) and MODIS (2015/2016 El Niño), respectively, is consistent with those obtained from MERRA-2 (Figs. 9a,b,d,e). Difference in total cloud fraction anomaly between the two El Niño events is physically linked to the precipitation anomaly distribution shown in Fig. 8. Both MERRA-2 and cloud observations exhibit this difference in cloud distribution between the two El Niño events (Figs. 9c,f).

Figure 10 shows the Walker circulation anomaly along the tropical Pacific and Indian Ocean for the three El Niño years. The well-known ascending motion anomaly over the central and eastern tropical Pacific, with anomalous subsidence over the western tropical Pacific, is clear in all three El Niño years (Figs. 10a–c). Figure 10 also demonstrates that the center of the anomalous anti-clockwise Walker circulation cell is located more to the west (close to 150°E) in the 2015/2016 El Niño than in the 1982/1983 and 1997/1998 El Niño events. Total cloud fraction exhibits the maximum anomaly (red shading) in the upper troposphere over the central to eastern tropical Pacific and the minimum (blue shading) over the western tropical Pacific and the Maritime Continent in all three El Niño years. The magnitude of the positive maximum cloud fraction in 2015/2016 appears comparable to that in 1997/1998 but smaller than that in the 1982/1983 El Niño. The location of the zero cloud fraction anomaly over the Pacific in 2015/2016 is ~160°E, which is west of the locations for the other two El Niño years. The zero cloud anomaly found over the CP generally corresponds with the center of the anomalous anti-clockwise Walker circulation cell.

276 The equatorial Indian Ocean exhibits a disorganized clockwise circulation cell in 2015/2016
277 compared to the other two El Niño years. The area of atmospheric subsidence anomaly is limited
278 to the Maritime Continent in 2015/2016 while the downward motion in the other two El Niño
279 years is found over a broad zonal band that covers the eastern Indian Ocean and the Maritime
280 Continent, with easterly flow in the lower-troposphere spanning the Indian Ocean longitudes.
281 This difference in atmospheric subsidence between the three El Niño years implies the relatively
282 small negative precipitation anomaly over the eastern tropical Indian Ocean in 2015/2016
283 compared to the other two El Niño years, as shown in the precipitation patterns of Fig. 7. Area-
284 averaged precipitation anomalies over the eastern tropical Indian Ocean, Indochina Peninsula,
285 and Maritime Continent (90°–140°E, 5S°–20°N) for 1982/1983, 1997/1998, and 2015/2016 El
286 Niño years are, respectively, –1.7, –2.1, and –0.9 mm d^{-1} (Table 1), indicating weaker drought
287 conditions in 2015/2016 than for the other two El Niño years. Associated with this relatively
288 weaker vertical circulation and drought conditions, the negative cloud fraction anomalies in
289 2015/2016 are also confined to the Maritime Continent, while they span the Maritime Continent
290 and the eastern Indian Ocean region (e.g., Bay of Bengal (60°–90°E)) in the 1982/1983 and
291 1997/1998 El Niño events.

292 We calculate diabatic temperature tendency (i.e., total diabatic heating/cooling) [K d^{-1}]
293 across the equatorial longitude-vertical plane. The diabatic temperature tendency here is due to
294 the multiple atmospheric processes that include moist, radiation, near-surface turbulence (e.g.,
295 sensible heat flux), and frictional dissipation of kinetic energy (e.g., gravity wave drag and
296 surface friction). The spatial structure in Fig. 11 is physically linked to the Walker circulation
297 anomaly shown in Fig. 10. It is apparent that the CP and EP are characterized by a heating while
298 a cooling is dominant over the WP, Maritime Continent, and eastern Indian Ocean (WMI)

299 region. MERRA-2 produces the maximum upper-tropospheric diabatic heating at ~150°W for
300 1982/1983 and 1997/1998, and west of it for 2015/2016. Comparison of the magnitude in each
301 process reveals that moist process that consists of all latent heating due to condensation and
302 evaporation plus the mixing by the parameterized convection explains the total diabatic heating
303 most significantly, followed by radiative process (Figure not shown). Also, the other terms are
304 about an order of magnitude smaller than that of the moist process.

305 Linked to the Walker circulation structure in the upper-troposphere (~200mb levels), the
306 velocity potential and divergent flow component at 200mb in Fig. 12 clearly demonstrates upper-
307 tropospheric divergence over the CP and EP and convergence over the WP for all three El Niño
308 cases. However, comparison between the three El Niño years indicates more convective activity
309 in 2015/2016 over the central tropical Pacific, where upper tropospheric divergence (blue
310 shading with divergence wind vector) is dominant (Fig. 12c). Upper-tropospheric convergence
311 (red shading) that indicates downward motion over the WMI region is relatively weaker in
312 2015/2016 than for the other two El Niño years. The 1997/1998 El Niño shows two centers of
313 divergence, one of them in the CP and the other in the far eastern Pacific. The center of
314 divergence in the far eastern Pacific would be due to the strong SST warming and convection
315 (see Fig. 11b) in that area in 1997/1998. Equatorial area between these two centers is
316 characterized by divergence as well.

317 In order to examine vertical circulation structures in the meridional direction around the
318 central tropical Pacific (180°–150°W), the Hadley circulation is compared between the three El
319 Niño years (Fig. 13). Rising motion is dominant within 10°S–0° for all three El Niño years.
320 However, the positive cloud fraction anomaly is largest in 2015/2016, implying the strongest
321 convective activity shifted west (toward the CP), compared to 1982/1983 and 1997/1998. The

branch of sinking motion in the subtropical latitude (20°–25°N) is also quite well organized stretching from the surface to the tropopause in 2015/2016, whereas the EP El Niño of 1997/1998 exhibits lower height of sinking motion. Better organized Hadley circulation over the CP in 2015/2016 could reflect changes in jet strength and enhancement of the positive phase of the Pacific North American (PNA) teleconnection (Jayawardena et al. 2011; Li and Wettstein 2012), which is understood to manifest better during the El Niño that includes the CP warming (Yu et al. 2012). This PNA teleconnection is further investigated in a companion study.

Hadley circulation structure is physically linked to diabatic temperature tendency and water vapor tendency as shown in Fig. 14. It is clear that diabatic heating (shaded) is more pronounced slightly north of the equator in the 2015/2016 El Niño, while the maximum heating is further to the south in the other two EP events, especially the 1997/1998 event as the 2015/2016 event has characteristics of both CP and EP warming (e.g., Figs. 8 and 9) (Xie and Yang 2014). This difference in the heating latitudes seems to imply that off-equatorial warm SST anomalies (e.g., in the SPCZ) contributed to the convections in 1997/1998 but the heating is more likely by the equatorial SST anomalies in 2015/2016. The tendency of water vapor in terms of specific humidity (contoured) exhibit the negative anomalies over the diabatic heating region due to active condensation processes. The largest amplitude in these two variables is situated in the tropical upper troposphere, possibly due to active condensation driven by moist convection. In contrast, diabatic cooling and gain of water vapor is found over the subtropics, the sinking branch of the Hadley circulation.

4. Transient Structure and Forcing

4.1 Time evolution of the equatorial Pacific SST

The time evolution of SST anomalies along the equatorial Pacific (averaged over 5°S–5°N) is plotted for the three strongest El Niño years. Figure 15 clearly shows that the positive SST anomaly (shaded red) is predominant over the central to eastern equatorial Pacific during the second half of the year as El Niño grows to maturity. On the other end, the WP is characterized by the negative SST anomaly. During the early part of 1982, 1997, and 2015 (January to March), the central to eastern equatorial Pacific SST starts off warmer in 2015 than in 1982 and 1997 because of a remnant of the weak warming over the equatorial Pacific that occurred in 2014 (Levine and McPhaden 2016). In fact, the SST maximum in 1997 is confined to the EP. The magnitude of the positive SST anomaly and its zonal contrast during the second half of 1982, 1997, and 2015 indicates that they are largest in 1997. All three El Niño events reach the maximum SST in boreal winter with the 1982/1983 El Niño reaching maturity in late December through early January, which is relatively later than the other two El Niño years. The 2015/2016 El Niño exhibits the earliest onset of El Niño decay as the positive SST anomalies in January and February 2016 are generally smaller than those in January–February 1983 and 1998. El Niño decay is further enhanced in April 2016 with a cold anomaly developing off the coast in the EP. May and June 2016 show further decay of the warm anomaly across the Niño3.4 and Niño3 regions. Although the 1982 El Niño starts development later than the other two El Niño events, the El Niño signal persists long after maturity as the large positive SST anomaly still remains in 1983. The 1997/1998 El Niño also exhibits larger positive SST anomaly in April 1998, compared to April 2016. However, the 1997/1998 El Niño significantly weakens after mid-May 1998, followed by a dramatic switch to a strong La Niña phase (Takayabu et al. 1999).

4.2 El Niño growth (Bjerknes feedback, westerly wind stress and MJO activity)

Westerly wind stress, WWB, and MJO activity, known to play a significant role in exciting

and growing El Niño (McPhaden et al. 1988; Kessler et al. 1995; Yu and Rienecker 1998; Kerr 1999; McGregor et al. 2015), are investigated in this section. Specifically, we examine the near-surface zonal wind, zonal wind stress, sub-surface water temperature, thermocline depth, ocean heat content, and MJO activity. The Hovmöller diagram in Figure 16 demonstrates that daily westerly wind anomalies at the 10m level (u10m) in the spring and early summer (MAMJ) of El Niño developing years are generally strongest in 1997. This is especially true for the WP region, where a series of the WWB can trigger the El Niño. For quantitative comparison among the events, we calculate the averaged magnitude of the daily westerly stress anomalies and u10m anomalies, respectively, over the WP (130°–160°E). The resulting values for the MAMJ period of 1982, 1997, and 2015 are 2.3, 4.3, and 2.7 [10^{-2} kg m^{-1} s^{-2}], and 2.0, 3.0, 2.3 [m s^{-1}], indicating that they are apparently largest in 1997, followed by 2015 and 1982. This relative difference in the westerly stress and u10m among the events is found to be consistent with the relative difference in the MJO amplitudes (1997 > 2015 > 1982) shown in Fig. 19d. Interestingly, it is found that the westerly stress and u10m anomalies prior to spring (January and February) are strongest in 2015. We also found that the occurrence of the daily time scale westerly stress anomalies during the first half of 2015 is as frequent as that in 1997.

During the second half of 1982, 1997, and 2015, it is clear that this u10m anomaly is weakest in the 2015/2016 event (Fig. 16). The averaged magnitudes of the daily westerly stress anomalies and u10m anomalies over the WP are 2.0, 1.8, and 1.5 [10^{-2} kg m^{-1} s^{-2}], and 1.9, 1.6, and 1.2 [m s^{-1}], indicating the largest magnitude in 1982. This largest westerly stress during the second half of 1982 contributes to the strong El Niño development, as the important role of the westerly stress anomaly in boreal summer is emphasized in Takahashi and Dewitte (2016). However, it is not easy to say that this largest westerly anomaly component is connected with the

391 MJO activity as the MJO is generally weak in the summer and fall of 1982 (see also Fig. 19).
392 The 1982/1983 event is one example that the connection between ENSO and the MJO is
393 complicated (Slingo et al. 1999).

394 The relatively weak westerly wind/stress anomalies during the second half of 2015 persist
395 through the following year (compare westerly wind anomalies between early 1983, 1998, and
396 2016), indicating the possibility of faster decay of the El Niño phase in 2016. Overall, despite the
397 earlier equatorial Pacific SST warming (Fig. 15c) and reasonably strong westerly anomaly
398 components in early 2015 (January and February), the El Niño growth in the subsequent period
399 is not as dramatic as 1997/1998. Especially, the u10m anomalies in the second half of 2015 are
400 weaker than those in the same calendar period in 1982 and 1997 across the equatorial Pacific
401 (Fig. 16). It implies that weaker growth of the 2015/2016 El Niño may be more associated with
402 the weaker Bjerknes feedback, consistent with the conclusion in L´Heureux et al. (2016).
403 Because the MJO (see also Fig. 19) and WWB activity was not so weak in the first half of 2015,
404 we suggest that they are not the primary cause of weaker growth of the 2015/2016 El Niño.

405 Relatively weak westerly wind anomaly and Bjerknes feedback in the second half of 2015
406 could be associated with the type of 2015/2016 El Niño where both the CP and EP warming was
407 involved. The eastward transport process of equatorial heat is not as efficient if the maximum sea
408 level anomaly is found west of the EP, while the EP El Niño is characterized by the east-west
409 seasaw pattern of sea level that facilitates the transport of equatorial heat to the east during the El
410 Niño growing stage (Kug et al. 2009). As shown in Fig. 17, the EP sub-surface water
411 temperature anomalies, which are dynamically linked to the near-surface westerly stress anomaly
412 that advects the WP warm pool into the CP and EP, are highest in 1997, when the equatorial
413 westerly wind anomalies (Fig. 16) are strong enough to promote an El Niño growth (second

column in Fig. 17), compared to 2015 (right column in Fig. 17). The sub-surface anomalies in December and January (El Niño peak) are more similar for the 1982/1983 and 1997/1998 event than for the 2015/2016 event, when the warm anomaly in the 2015/2016 event is not as strong as for 1982/1983 and 1997/1998. Warmer sub-surface water is more widely accumulated over the EP in 1997, along with the strong negative anomaly over the WP. As it was also presented in Fig. 5, the thermocline depth in the EP is larger in 1997 with more flattening of the slope from west to east. More active excitement of downwelling eastward Kelvin waves is expected for 1997 along the thermocline across the equatorial Pacific (McPhaden 1999). In contrast, zonal contrast in sub-surface water temperature is relatively weaker in 2015 (right column in Fig. 17) than in 1997, in association with relatively weak westerly wind anomalies that can induce accumulation of warm water over the EP.

Consistent with the evolution feature in Figs. 15–17, accumulation of the upper ocean heat content in the eastern side of the Pacific and its zonal contrast during the El Niño maturity is strongest in 1997/1998 (Fig. 18). Timing of the peak in the zonal contrast is latest (Dec 1982 – Jan 1983) in the 1982/1983 event due to a later start of the El Niño development. During the early 1982, 1997, and 2015, positive heat content anomaly greater than 1°C is found in the WP and CP, where it is advected into the EP as the ENSO involves a discharge of warm water volume along the equator (Zebiak 1989; Meinen and McPhaden, 2000). While MERRA-Ocean shows a weak heat content anomaly for the early 1982, it is important to note that the uncertainty in the ocean state estimate is significantly larger for the 1982/1983 event than for the 1997/1998 and 2015/2016 events. Prior to the advent of the Tropical Atmosphere Ocean (TAO) array (Hayes et al. 1986), the ocean observing system consists of SST and very sparse in-situ measurements.

Because the WWB tends to be embedded within the active phase of the MJO (Yu and Rienecker 1998), we examine the propagation of the MJO along the tropical Pacific using the NCEP/CPC MJO indices and Wheeler and Hendon indices (Wheeler and Hendon 2004). The CPC MJO indices are constructed by regressing 200mb velocity potential onto the first several leading modes associated with the MJO (see Xue et al. (2002) for methodology). Time evolution of the MJO in Fig. 19 clarifies that eastward propagation of the MJO in spring is more pronounced in 1997, compared to 2015. Note that, because of the climatological nature that the MJO usually weakens in boreal summer, the MJO signals are frequent before summer. Early 1997 period exhibits the most frequent eastward passages of the MJO-related convection (Figs. 19b,d), followed by 2015 (Figs. 19c,d). In 1982, a few eastward MJO propagations are found in spring (Fig. 19a), but their intensity is lower than that in the other events (Fig. 19d). Figures 15–19 overall suggest that, while the 1997/1998 El Niño combines well with the strong WWB and MJO activity in the first half of the year, another strong EP El Niño in 1982 is developed through the enhanced westerly wind stress in the second half of 1982. In early 2015, the WWB and MJO are not weak (they are weak in the second half of the year) and the equatorial Pacific is warmer than the other events, but the El Niño growth is less dramatic than the 1997/1998 event, possibly connected with the weaker Bjerknes feedback.

5. Concluding remarks and discussion

This study overviews characteristic features of the atmosphere and ocean during the three strongest El Niño events on record, namely the events that occurred in 1982/1983, 1997/1998, and 2015/2016, using MERRA-2.

The structure of the 2015/2016 El Niño, with a maximum SST anomaly in the Niño 3.4

region with warming extending to the West of the dateline and only a weak impact on SST in the far EP, displays characteristics of both EP and CP type El Niño. This is also evidenced by various atmospheric structures, including Walker circulation, vertical structure of diabatic heating tendency, cloud fraction and precipitation. While the temperature anomalies in the Niño3.4 region were largest in the 2015/2016 event (on the basis of the Reynolds OISST and MERRA-Ocean data used in this study), the 1997/1998 event had the largest overall impacts, with warm anomalies extending to the coast of South America. The 1997/1998 event thus showed the larger zonal contrast in SST anomaly along the equatorial Pacific than the 2015/2016 event. The largest precipitation amount over the central tropical Pacific is found in the 2015/2016 El Niño, while the largest precipitation over the EP occurred in 1997/1998. Regarding the region of drought conditions, downward Walker circulation over the WMI region and associated decrease in cloudiness is less pronounced in 2015/2016 relative to the 1997/1998 El Niño case. Area-averaged precipitation anomalies (Table 1) support our conclusion that the 2015/2016 El Niño was in a less severe drought condition over the WMI region.

Though the El Niño signal in terms of the CP and EP warming is detected earlier in 2015, growth of El Niño from the early through mature stage over the tropics is more dramatic in the 1997/1998 El Niño. Sub-surface water temperature anomaly and the slope of the thermocline along the equatorial Pacific support this conclusion. It is not easy to clearly demonstrate the difference in strength between the 1982/1983 and 2015/2016 El Niño. However, a clear difference is that the onset of the 1982/1983 El Niño is later than the 2015/2016 El Niño, but the El Niño signal remains longer after maturity, compared to the 2015/2016 El Niño.

Based on the results in this study, we suggest that the relatively slow growth of the 2015/2016 El Niño over the tropics, compared to the 1997/1998 El Niño, can be attributed to

weaker Bjerknes feedback. Associated major features in the observations are weaker westerly wind anomalies, less eastward advection of the warm SST, less accumulation of warm sub-surface ocean water, and a shallower thermocline over the EP, compared to 1997. Location of the maximum SST anomalies is also shifted west of those in the 1982/1983 and 1997/1998 events.

Although the El Niño growth is not as dramatic as the other strong events, the 2015/2016 event is accepted as the top three strongest one that attained an extraordinary warming over the central to eastern equatorial Pacific. We compare the upper-ocean heat content and SST in the 2015-2016 El Niño with those for the other CP events that occurred in the 2000s (e.g., 2004/2005 and 2009/2010). The 2015/2016 event has higher heat content across the equatorial Pacific at El Niño initial stage than the other selected 2000s events (Figure not shown). This condition in early 2015 indicates a high potential to be a strong El Niño once the strong westerly wind stress is imposed (Meinen and McPhaden 2000; Fedorov et al. 2015). Fedorov et al. (2015) also demonstrated that weak westerly stress anomalies lead to a maximum warming in the CP. Conclusively, we suggest that the strong ocean heat content distribution in the 2015/2016 El Niño onset period provides a favorable condition for developing the strong El Niño SST, but the weak Bjerknes feedback during the El Niño developing stage is not able to locate the maximum El Niño SST anomalies in the far EP. Takahashi and Dewitte (2016) also suggested the importance of non-linear convective feedback to account for the SST and sub-surface warming across the EP.

We know that multiple WWBs and MJOs help to develop the largest El Niño events (McPhaden 1999). However, accurate prediction of the El Niño strength in early calendar months is very challenging because the prediction of the MJO intensity and initiation by current forecast models is still poor (Kerr 1999; Bechtold et al. 2008; Kim et al. 2009; Kim et al. 2014;

506 Vitart 2014). In fact, the possibility of the very strong 2015/2016 El Niño was not foreseen until
507 the middle of 2015. Model forecasts in January 2015 predicted that weak warm conditions over
508 the tropical Pacific would decay in Northern Hemisphere spring (McPhaden 2015). The problem
509 raised here suggests that the growth of ENSO and its strength strongly depend on sub-seasonal
510 atmosphere/ocean variability.

511 Additionally, this study identified that SST and 2mT anomalies in 2015/2016 are positive
512 and generally greater than 1982/1983 and 1997/1998 over the majority of the WMI and
513 extratropical Pacific (see Fig. 20). This uncommon widespread warming is suggested to be a
514 combination of the following two features. First, we found that an upward trend in 2mT over the
515 past 37 years (1979 – 2015) is greater over the WMI than over the eastern tropical Pacific. The
516 calculated linear trend over those two regions (WMI (60°–150°E, 10S°–10°N) vs. eastern
517 tropical Pacific (150°–70°W, 10S°–10°N)) is found to be, +0.19 decade^{-1} and +0.10 decade^{-1},
518 respectively. It suggests that higher temperatures over the WMI in 2015/2016 can be attributed to
519 a larger decadal warming trend over that region (Cravatte et al. 2009). Secondly, the nature of
520 the El Niño that includes the CP warming such as 2015/2016 event is known to drive warming
521 extending west of the dateline and extratropical Pacific (Larkin and Harrison 2005; Kao and Yu
522 2009), compared to the EP El Niño.

523 In summary, the reanalysis datasets reveal that the three strong El Niño events each have
524 unique characteristics in their oceanic and atmospheric structures. Issues related to their
525 individual dynamical evolution and the possible impacts of trends in climate forcing on El Niño
526 development are evident in the reanalyses, but clearly a complete understanding of each of these
527 events remains a topic for future study.

528

Acknowledgments

Colleagues in the production group of the GMAO, especially Gi-Kong Kim and Rob Lucchesi, have tirelessly produced the MERRA-2 reanalysis. Jelena Marshak and Anna Borovikov produce the oceanic analysis. High-performance computing resources are provided by the NCCS at NASA GSFC.

References

Ashok, K., C.-Y. Tam, and W.-J. Lee, 2009: ENSO Modoki impact on the Southern Hemisphere storm track activity during extended austral winter. *Geophys. Res. Lett*., **36**, L12705, doi:10.1029/2009GL038847.

Bechtold, P., M. Köhler, T. Jung, F. Doblas-Reyes, M. Leutbecher, M. J. Rodwell, F. Vitart, and G. Balsamo, 2008: Advances in simulating atmospheric variability with the ECMWF model: From synoptic to decadal time-scales. *Quart. J. Roy. Meteor. Soc*., **134**, 1337-1351, doi:10.1002/qj289.

Bell, G. D., M. Halpert, and M. L´Heureux, 2016: ENSO and the tropical Pacific. *Bull. Amer. Meteor. Soc.*, **97**(8), S93-S98.

Bosilovich, M. G., and coauthors, 2015: MERRA-2: Initial evaluation of the climate. *NASA/TM–2015–104606*, Vol. **43**, 139 pp.

Cravatte, S., T. Delcroix, D. Zhang, M. McPhaden, and J. Leloup, 2009: Observed freshening and warming of the western Pacific warm pool. *Clim. Dyn*., **33**(4), 565-589, doi:10.1007/s00382-009-0526-7.

Dee, D. P., and coauthors, 2011 The ERA-Interim reanalysis: configuration and performance of the data assimilation system. *Quart. J. Royal Meteorol. Soc*., **137**, 553–597, doi:10.1002/qj.828.

Fedorov, A. V., S. Hu, M. Lengaigne, and E. Guilyardi, 2015: The impact of westerly wind bursts and ocean initial state on the development, and diversity of El Niño events. *Clim. Dyn*., **44**(5), 1381-1401, doi:10.1007/s00382-014-2126-4.

Gelaro, R., and coauthors, 2016: The Modern-Era Retrospective Analysis for Research and Applications, Version-2 (MERRA-2). Submitted to *J. Climate*.

Global Modeling and Assimilation Office (GMAO), 2015a: MERRA-2 tavgM_2d_slv_Nx: 2d, Monthly mean, Time-Averaged, Single-Level, Assimilation, Assimilated Meteorological Fields, version 5.12.4, Greenbelt, MD, USA: Goddard Space Flight Center Distributed Active Archive Center (GSFC DAAC), Accessed Aug 2016. doi:10.5067/AP1B0BA5PD2K.

Global Modeling and Assimilation Office (GMAO), 2015b: MERRA-2 tavgM_2d_flx_Nx: 2d, Monthly mean, Time-Averaged, Single-Level, Assimilation, Surface Flux Diagnostics, version 5.12.4, Greenbelt, MD, USA: Goddard Space Flight Center Distributed Active

Archive Center (GSFC DAAC), Accessed Aug 2016. doi:10.5067/0JRLVL8YV2Y4.

Global Modeling and Assimilation Office (GMAO), 2015c: MERRA-2 instM_3d_asm_Np: 3d, Monthly mean, Instantaneous, Pressure-Level, Assimilation, Assimilated Meteorological Fields, version 5.12.4, Greenbelt, MD, USA: Goddard Space Flight Center Distributed Active Archive Center (GSFC DAAC), Accessed Aug 2016. doi:10.5067/2E096JV59PK7.

Global Modeling and Assimilation Office (GMAO), 2015d: MERRA-2 tavgM_3d_tdt_Np: 3d, Monthly mean, Time-Averaged, Pressure-Level, Assimilation, Temperature Tendencies, version 5.12.4, Greenbelt, MD, USA: Goddard Space Flight Center Distributed Active Archive Center (GSFC DAAC), Accessed Aug 2016. doi:10.5067/VILT59HI2MOY.

Global Modeling and Assimilation Office (GMAO), 2015e: MERRA-2 tavgM_3d_qdt_Np: 3d, Monthly mean, Time-Averaged, Pressure-Level, Assimilation, Moist Tendencies, version 5.12.4, Greenbelt, MD, USA: Goddard Space Flight Center Distributed Active Archive Center (GSFC DAAC), Accessed Aug 2016. doi:10.5067/2ZTU87V69ATP.

Global Modeling and Assimilation Office (GMAO), 2015f: MERRA-2 tavgM_3d_rad_Np: 3d, Monthly mean, Time-Averaged, Pressure-Level, Assimilation, Cloud and Radiative Fields, version 5.12.4, Greenbelt, MD, USA: Goddard Space Flight Center Distributed Active Archive Center (GSFC DAAC), Accessed Aug 2016. doi:10.5067/H3YGROBVBGFJ.

Global Modeling and Assimilation Office (GMAO), 2015g: MERRA-2 tavgM_2d_csp_Nx: 2d, Monthly mean, Time-Averaged, Single-Level, Assimilation, Cloud Fields, version 5.12.4, Greenbelt, MD, USA: Goddard Space Flight Center Distributed Active Archive Center (GSFC DAAC), Accessed Aug 2016. doi:10.5067/BZPOTGJOQKLU.

Gould, J., and coauthors, 2004: Argo profiling floats bring new era of in-situ ocean observations. *Eos*, **85(19)**.

Guenther, B., W. Barnes, E. Knight, J. Barker, J. Harnden, R. Weber, M. Roberto, G. Godden, H. Montgomery, and P. Abel, 1996:. MODIS calibration: A brief review of the strategy for the at-launch calibration approach. *J. Atmos. Ocean Tech.*, **13(2)**, 274-285.

Hayes, S.P., D.W. Behringer, M. Blackmon, D.V. Hansen, N.C. Lau, A. Leetmaa, S.G.H. Philander, E.J. Pitcher, C.S. Ramage, E.M. Rasmusson, E.S. Sarachik, and B.A. Taft, 1986: The Equatorial Pacific Ocean Climate Studies (EPOCS) Plans: 1986-1988. *Eos Trans. AGU, 67*, 442-444.

Huang. B., M. L'Heureux, Z.-Z. Hu, and H.-M. Zhang (2016), Ranking the strongest ENSO

events while incorporating SST uncertainty, *Geophys. Res. Lett.*, **43**, 9165–9172, doi:10.1002/2016GL070888.

Huffman, G. J., R. F. Adler, D. T. Bolvin, G. Gu, E. J. Nelkin, K. P. Bowman, E. F. Stocker, and D. B. Wolff, 2007: The TRMM multi-satellite precipitation analysis: Quasi-global, multi-year, combined-sensor precipitation estimates at fine scale. *J. Hydrometeor*., **8**, 33-55.

Huffman, G. J., D. T. Bolvin, D. Braithwaite, K. Hsu, R. Joyce, C. Kidd, E. J. Nelkin, and P. Xie, 2015: NASA Global Precipitation Measurement (GPM) Integrated Multi-satelliteE Retrievals for GPM (IMERG). *https://pmm.nasa.gov/sites/default/files/document_files/IMERG_ATBD_V4.5_0.pdf*.

Jayawardena I. M. S., Y.-L. Chen, A. J. Nash, and K. Kodama, 2011: A comparison of three prolonged periods of heavy rainfall over the Hawaiian islands. J. Appl. Meteor.Climatol., 51, 722-744, doi:10.1175/JAMC-D-11-0133.1.

Kao, H.-Y., and J.-Y. Yu, 2009: Contrasting Eastern-Pacific and Central-Pacific types of ENSO. *J. Climate*, **22**, 615-632, doi:10.1175/2008JCLI2309.1.

Keppenne, C. L., M. M. Rienecker, J. P. Jacob, and R. Kovach, 2008: Error covariance modeling in the GMAO ocean ensemble Kalman filter. *Mon. Wea. Rev*., **136**, 2964-2982, doi:10.1175/2007MWR2243.1.

Kerr, R. A., 1999: Does a globe-girdling disturbance jigger El Niño? *Science*, **285**, 322-323, doi:10.1126/science.285.5426.322.

Kessler W. S., M. J. PcPhaden, and K. M. Weickmann, 1995: Forcing of intraseasonal Kelvin waves in the equatorial Pacific. *J. Geophys. Res*., **100(C6)**, 10613-10631, doi:10.1029/95JC00382.

Kim, D., and Coauthors, 2009: Application of MJO simulation diagnostics to climate models. *J. Climate*, **22**, 6413-6436, doi:10.1175/2009JCLI3063.1.

Kim, H.-M., P. J. Webster, V. E. Toma, and D. Kim, 2014: Predictability and prediction skill of the MJO in two operational forecasting systems. *J. Climate*, **27**, 5364-5378, doi:10.1175/JCLI-D-13-00480.1.

Kug, J.-S., F.-F. Jin, and S.-I. An, 2009: Two-types of El Niño events: Cold tongue El Niño and warm pool El Niño. *J. Climate*, **22**, 1499–1515, doi:10.1175/2008JCLI2624.1.

Larkin, N. K., and D. E. Harrison, 2005: Global seasonal temperature and precipitation anomalies during El Niño autumn and winter. *Geophys. Res. Lett*., **32**, L16705,

628 doi:10.1029/2005GL022860.
629 Larson, S. M., and B. P. Kirtman, 2015: An alternate approach to ensemble ENSO forecast
630 spread. *Geophys. Res. Lett.*, **42**, 9411-9415, doi:10.1002/2015GL066173.
631 Levine, A. F. Z., and M. J. McPhaden, 2016: How the July 2014 easterly wind burst gave the
632 2015-2016 El Niño a head start. *Geophys. Res. Lett*, **43**, doi:10.1002/2016GL69204.
633 L´Heureux, M., K. Takahashi, A. Watkins, A. Barnston, E. Becker, T. Di Liberto, F. Gamble, J.
634 Gottschalck, M. Halpert, B. Huang, K. Mosquera-Vásquez, and A. Wittenberg, 2016:
635 Observing and predicting the 2015-16 El Niño. *Bull. Amer. Meteor. Soc.*
636 doi:10.1175/BAMS-D-16-0009.1, in press.
637 Li, C., and J. J. Wettstein, 2012: Thermally driven and eddy driven jet variability in reanalysis. *J.*
638 *Climate*, **25**, 1587-1596, doi:10.1175/JCLI-D-11-00145.1.
639 Maslanik, J., and J. Stroeve. 1999: *Near-Real-Time DMSP SSMIS Daily Polar Gridded Sea Ice*
640 *Concentrations, Version 1*. (http://nsidc.org/data/nsidc-0081), Boulder, Colorado USA.
641 NASA National Snow and Ice Data Center Distributed Active Archive Center. doi:
642 10.5067/U8C09DWVX9LM.
643 McGregor, S., A. Timmermann, F.-F. Jin, and W. S. Kessler, 2015: Charging El Niño with off-
644 equatorial westerly wind events. *Clim. Dyn*., 1-18, doi:10.1007/s00382-015-2891-8.
645 McPhaden, M. J., H. P. Freitag, S. P. Hayes, B. A. Taft, Z. Chen, and K. Wyrtki, 1988: The
646 response of the equatorial Pacific Ocean to a westerly wind burst in May 1986. *J. Geophys.*
647 *Res*., **93(C9)**, 10589-10603.
648 McPhaden, M. J., 1999: Genesis and evolution of the 1997-98 El Niño. *Science*, **283**, 950-954,
649 doi:10.1126/science.283.5404.950.
650 McPhaden, M. J., 2015: Playing hide and seek with El Niño. *Nature Climate Change*, **5**, 791-
651 795, doi:10.1038/nclimate2775.
652 Meehl, G. A., A. Hu, and H. Teng, 2016: Initialized decadal prediction for transition to positive
653 phase of the Interdecadal Pacific Oscillation. *Nat. Commun*., **7**, 11718,
654 doi:10.1038/ncomms11718.
655 Meinen, C. S., M. J. McPhaden, 2000: Observations of warm water volume changes in the
656 equatorial Pacific and their relationship to El Niño and La Niña. *J. Climate*, **13**, 3551-3559.
657 Min, Q., J. Su, R. Zhang, and X. Rong, 2015: What hindered the El Niño pattern in 2014?
658 *Geophys. Res. Lett*., **42**, 6762-6770, doi:10.1002/2015GL064899.

659 Molod, A., L. Takacs, M. Suarez, J. Bacmeister, 2015: Development of the GEOS-5
660 Atmospheric General Circulation Model: Evolution from MERRA to MERRA2. *Geosci.*
661 *Model Dev.* **8**, 1339-1356, doi:10.5194/gmd-8-1339-2015.
662 Moorthi, S., and M. J. Suarez, 1992: Relaxed Arakawa-Schubert: A parameterization of moist
663 convection for general circulation models. *Mon. Wea. Rev.*, **120**, 978-1002.
664 Rayner, N. A., and coauthors, 2003: Global analyses of sea surface temperature, sea ice, and
665 night time air temperature since the late nineteenth century. *J. Geophys. Res*., **108,** (D14),
666 4407, doi:10.1029/2002JD002670.
667 Reynolds, R. W., T. M. Smith, C. Liu, D. B. Chelton, K. S. Casey, and M. G. Schlax, 2007:
668 Daily high-resolution-blended analyses for sea surface temperature. *J. Climate*, **20**, 5473-
669 5496, doi:10.1175/2007JCLI1824.1.
670 Schiffer, R.A., and Rossow, W.B., 1983: The International Satellite Cloud Climatology Project
671 (ISCCP): The first project of the World Climate Research Programme. *Bull. Amer. Meteor.*
672 *Soc*., **64**, 779-784
673 Slingo, J. M., D. P. Rowell, K. R. Sperber, and F. Nortley, 1999: On the predictability of the
674 interannual behavior of the Madden-Julian oscillation and its relationship with El Niño.
675 *Quart. J. Roy. Meteor. Soc.*, **125**, 583-609, doi:10.1002/qj.49712555411.
676 Takahashi, K., and B. Dewitte, 2016: Strong and moderate nonlinear El Ninño regimes. *Clim.*
677 *Dyn*., **46** (5), 1627–1645, doi:10.1007/s00382-015-2665-3.
678 Takayabu, Y. N. ,T. Iguchi, M. Kachi, A. Shibata, and H. Kanzawa, 1999: Abrupt termination of
679 the 1997-98 El Niño in response to a Madden-Julian oscillation. *Nature*, 402, 279-282.
680 Vernieres, G., M. Rienecker, R. Kovach, and C. Keppenne, 2012: The GEOS-iODAS:
681 Description and Evaluation. *NASA Technical Report Series on Global Modeling and Data*
682 *Assimilation, NASA TM—2012-104606*, Vol. **30**, 61 pp.
683 Vitart, F., 2014: Evolution of ECMWF sub-seasonal forecast skill scores. *Quart. J. Royal.*
684 *Meteor. Soc*., 140, 1889-1899, doi:10.1002/qj2256.
685 Wang, W., and M. J. McPhaden, 2000: The surface layer heat balance in the equatorial Pacific
686 ocean. Part II: Interannual variability. *J. Phys. Oceanogr*., **30**, 2989-3008.
687 Weng, H., S. K. Behera, and T. Yamagata, 2009: Anomalous winter climate conditions in the
688 Pacific rim during recent El Niño Modoki and El Niño events. *Clim. Dyn*., **32**, 663–674,
689 doi:10.1007/s00382-008-0394-6.

690 Wheeler, M. C., and H. H. Hendon, 2004: An all-season real-time multivariate MJO index:
691 Development of an index for monitoring and prediction. Mon. Wea. Rev., 132, 1917-1932,
692 doi:10.1175/1520-0493(2004)132<1917:AARMMI>2.0.CO;2.
693 Wolter, K., and M. S. Timlin, 1998: Measuring the strength of ENSO events - how does 1997/98
694 rank? *Weather*, **53,** 315-324.
695 Xie, R., and Y. Yang, 2014: Revisiting the latitude fluctuations of the eastern Pacific ITCZ
696 during the central Pacific El Niño. *Geophys. Res. Lett.*, **41**, 7770-7776,
697 doi:10.1002/2014GL061857.
698 Xue, Y., W. Higgins, and V. Kousky, 2002: Influences of the Madden Julian Oscillations on
699 temperature and precipitation in North America during ENSO-neutral and weak ENSO
700 winters. *A workshop on Prospects for Improved Forecasts of Weather and Short-term*
701 *Climate Variability on Subseasonal Time Scales*, NASA/Goddard Space Flight Center, April
702 16-18.
703 Yeh, S.-W., J.-S. Kug, B. Dewitte, M.-H. Kwon, B. P. Kirtman, and F.-F. Jin, 2009: El Niño in a
704 changing climate. *Nature*, **461**, 511-514, doi:10.1038/nature08316.
705 Yu, J.-Y., Y. Zou, S.-T. Kim, and T. Lee, 2012: The changing impact of El Niño on US winter
706 temperatures. *Geophys. Res. Lett.*, **39**, L15702, doi:10.1029/2012GL052483.
707 Yu, L., and M. M. Rienecker, 1998: Evidence of an extratropical atmospheric influence during
708 the onset of the 1997-98 El Niño. *Geophys. Res. Lett.*, **25(18)**, 3537-3540.
709 Zebiak, S. E., 1989: Oceanic heat content variability and El Niño cycles. *J. Phys. Oceanogr.*, **19**,
710 475-486.
711

712 **Table 1**. Area-averaged two-meter temperature (2m T °C) and precipitation (Precip, mm d^{-1})
713 anomalies in several tropical regions during the El Niño winters of 1982/1983, 1997/1998, and
714 2015/2016. The regions, indicated in the left column, are Indian Ocean, Indochina Peninsula and
715 Maritime Continent (INDMC: 90°–140°E, 5°S–20°N), Western Pacific (WP: 140°–160°E, 5°S–
716 5°N), Central Pacific (CP: 160°E–150°W, 5°S–5°N), Eastern Pacific (EP: 150°–80°W, 5°S–
717 5°N), and tropical South America (SA: 80°–30°W, 10°S–5°N).

Region	1982/1983		1997/1998		2015/2016	
	2m T	Precip	2m T	Precip	2m T	Precip
INDMC	0.0	–1.7	0.6	–2.1	0.7	–0.9
WP	–0.4	–3.4	0.0	–3.9	0.3	–1.3
CP (Niño 4 and part of Niño3.4)	0.3	4.0	0.6	2.8	1.2	8.7
EP (Niño3 and Niño1+2)	2.2	5.3	2.6	8.5	2.2	2.5
SA	0.6	–1.4	1.1	–1.1	1.4	–1.6

718

719

Figure Captions

Figure 1. Sea surface salinity in-situ observations for December 1982 (top), 1997 (middle), and 2015 (bottom). Observations are from Argo drifting buoys, XBT and CTD profilers, and TAO, PIRATA, and RAMA moorings.

Figure 2. Time series of sea surface temperature (SST) anomaly averaged over a) Niño 4, b) Niño 3.4, c) Niño 3, and d) Niño 1+2 regions for the period 1982–2016. The red/blue shaded curves show the Reynolds SST while the solid curve represents the analyzed values from GEOS-5.

Figure 3. SST over the tropical Pacific from MERRA Ocean (left column) for December 1982 (first row), December 1997 (second row) and December 2015 (third row). The highlighted boxes from West to East are Niño4, Niño 3.4 (white), Niño 3, and Niño1+2.

Figure 4. Difference fields over the tropical Pacific from MERRA Ocean for December 2015 minus 1997 (top row), December 2015 minus 1982 (second row), and December 1997 minus 1982 (bottom row). The difference fields shown are SST (left column) and zonal ocean current velocity (right column). The highlighted boxes from West to East are Niño4, Niño 3.4, Niño 3, and Niño1+2.

Figure 5. Comparison of longitude-depth sections of sub-surface water temperature (°C) along the equator during the El Niño mature stage in December of 1982, 1997 and 2015. The bold black line depicts the location of 20°C isotherm.

Figure 6. Difference fields in sea surface salinity (SSS) (shaded) over the tropical Pacific from MERRA Ocean for DJF 2015 minus 1997 (top row), DJF 2015 minus 1982 (second row), and DJF 1997 minus 1982 (bottom row). Contoured is the same as SSS but for precipitation minus evaporation from MERRA-2.

Figure 7. Total precipitation anomalies [mm d^{-1}] in boreal winter (December, January, and February) of the three strongest El Niño years. Dashed boxes denote the areas where area-averaged 2 meter air temperature and precipitation anomalies are calculated (see Table 1).

Figure 8: Difference in total precipitation [mm d^{-1}] between 2015/2016 and 1997/1998 El Niño (2015/2016 minus 1997/1998) from MERRA-2 (top panel) and TRMM and IMERG observation (bottom panel).

Figure 9: MERRA-2 total cloud fraction anomalies in boreal winter of 1997/1998 and 2015/2016 El Niño events and their comparison with observations from the ISCCP (top panel,

1997/1998 El Niño) and the MODIS (middle panel, 2015/2016 El Niño). The bottom panel represents the difference in total cloud fraction anomaly between the two El Niño events from MERRA-2 (lower-left) and MODIS/ISCCP observation (lower-right).

Figure 10. Longitude-pressure [mb] sections along the equator (10°S-10°N averaged) showing the Walker circulation (streamlines) and total cloud fraction anomalies (shaded) over the Indian Ocean, Maritime Continent, and Pacific. The plots are for the boreal winters (December through February) of (a) 1982/1983, (b) 1997/1998, and (c) 2015/2016.

Figure 11. Same as Figure 10 but for the total diabatic temperature tendency [K d^{-1}] anomaly. This value is the outcome of the multiple thermodynamic processes that include moist (e.g., latent heat and convection), radiation, near-surface turbulence (e.g., sensible heat flux), and frictional dissipation of kinetic energy (e.g., gravity wave drag and surface friction). Note that the moist process plays the most substantial role in determining this diabatic temperature tendency over the tropics.

Figure 12. The velocity potential [10^6 m^2s^{-1}] (shaded) and the divergent wind component [m s^{-1}] (vector) in the upper-troposphere (200mb) in the boreal winters of (a) 1982/1983, (b) 1997/1998, and (c) 2015/2016.

Figure 13. Latitude-pressure sections showing the Hadley circulation (streamline) and total cloud fraction anomalies (shaded), averaged over the longitude range between 150°W and the dateline. Plots are shown for the boreal winters of (a) 1982/1983, (b) 1997/1998, and (c) 2015/2016.

Figure 14. Same as Figure 13 but for the total diabatic temperature tendency [K d^{-1}] (shaded) and specific humidity tendency [10^{-4} kg kg^{-1} d^{-1}] due to moist process (contoured).

Figure 15. Time evolution of the equatorial Pacific sea surface temperature anomalies (averaged over 5°S–5°N) during the three strongest El Niño years, 1982/1983 (left), 1997/1998 (middle), and 2015/2016 (right). The x-axis represents longitude whereas the y-axis is the time in month.

Figure 16. Time evolution of the daily equatorial 10-meter zonal wind anomalies [m s^{-1}] (averaged over 5°S–5°N) during the three strongest El Niño years, 1982/1983 (left), 1997/1998 (middle), and 2015/2016 (right). The x-axis represents longitude whereas the y-axis is the time in month.

Figure 17. Sub-surface water temperature anomalies [°C] along the equatorial Pacific for the 1982/1983 (left), 1997/1998 (middle), and 2015/2016 (right) ENSO events as the El Niño

approaches maturity from October (top) to the beginning of the decay (bottom). The y-axis on the sub-surface water temperature anomaly pattern is the ocean depth in meters.

Figure 18. Same as Fig. 15 but for the ocean heat content anomaly

Figure 19. Upper: Time evolution of the MJO propagation along the equatorial Pacific for the period 1982 (left), 1997 (middle), and 2015 (right). The blueish (reddish) color represents the enhanced (suppressed) MJO-related convection. Lower: Time series of the MJO amplitude from the Wheeler and Hendon index. Black, blue, and red curve represents 1982, 1997, and 2015, respectively. The x-axis represents longitude whereas the y-axis is the time in month.

Figure 20. 2 meter air temperature anomalies [°C] in boreal winter (December, January, and February) of the three strongest El Niño years.

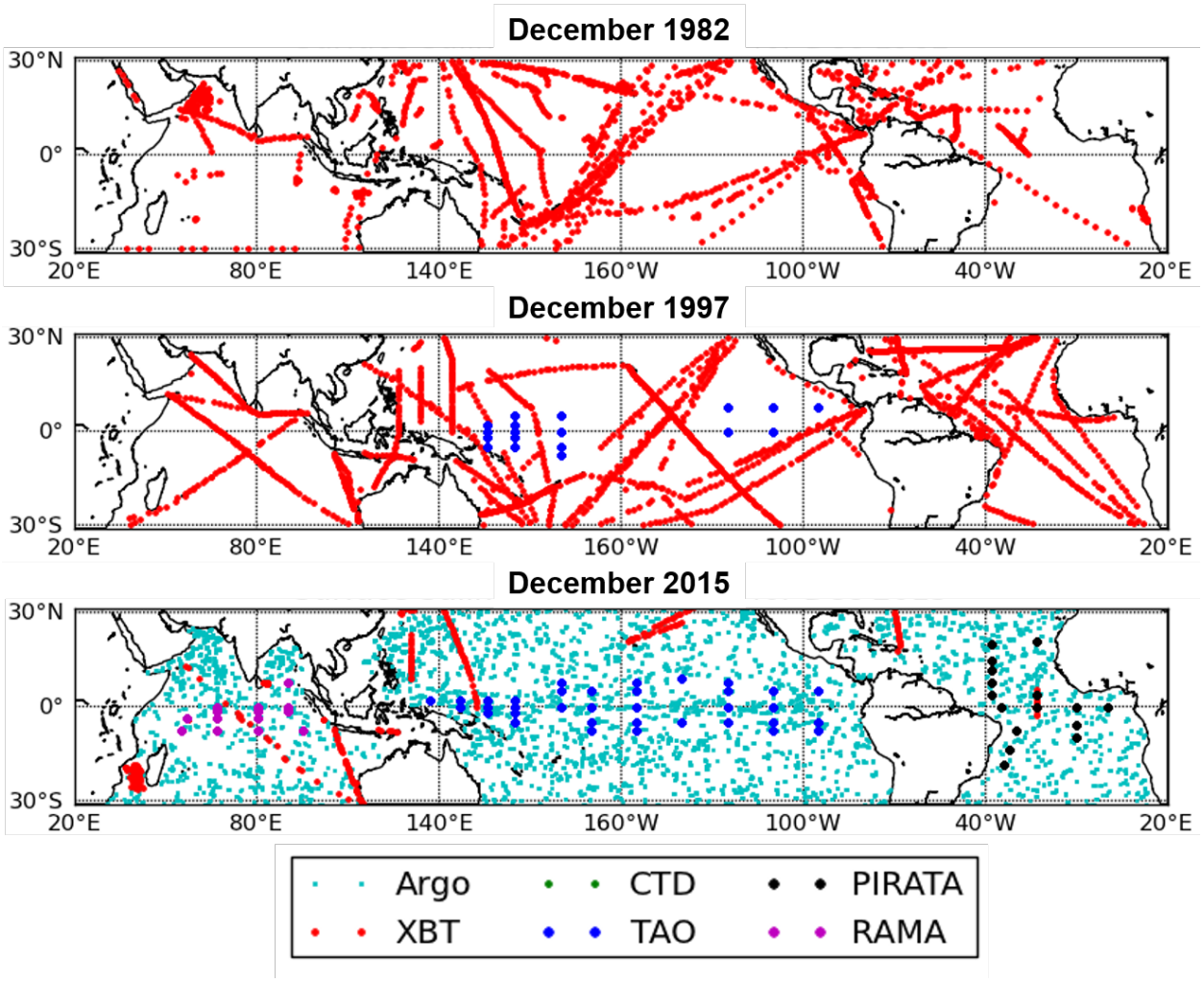

Figure 1. Sea surface salinity *in-situ* observations for December 1982 (top), 1997 (middle), and 2015 (bottom). Observations are from Argo drifting buoys, XBT and CTD profilers, and TAO, PIRATA, and RAMA moorings.

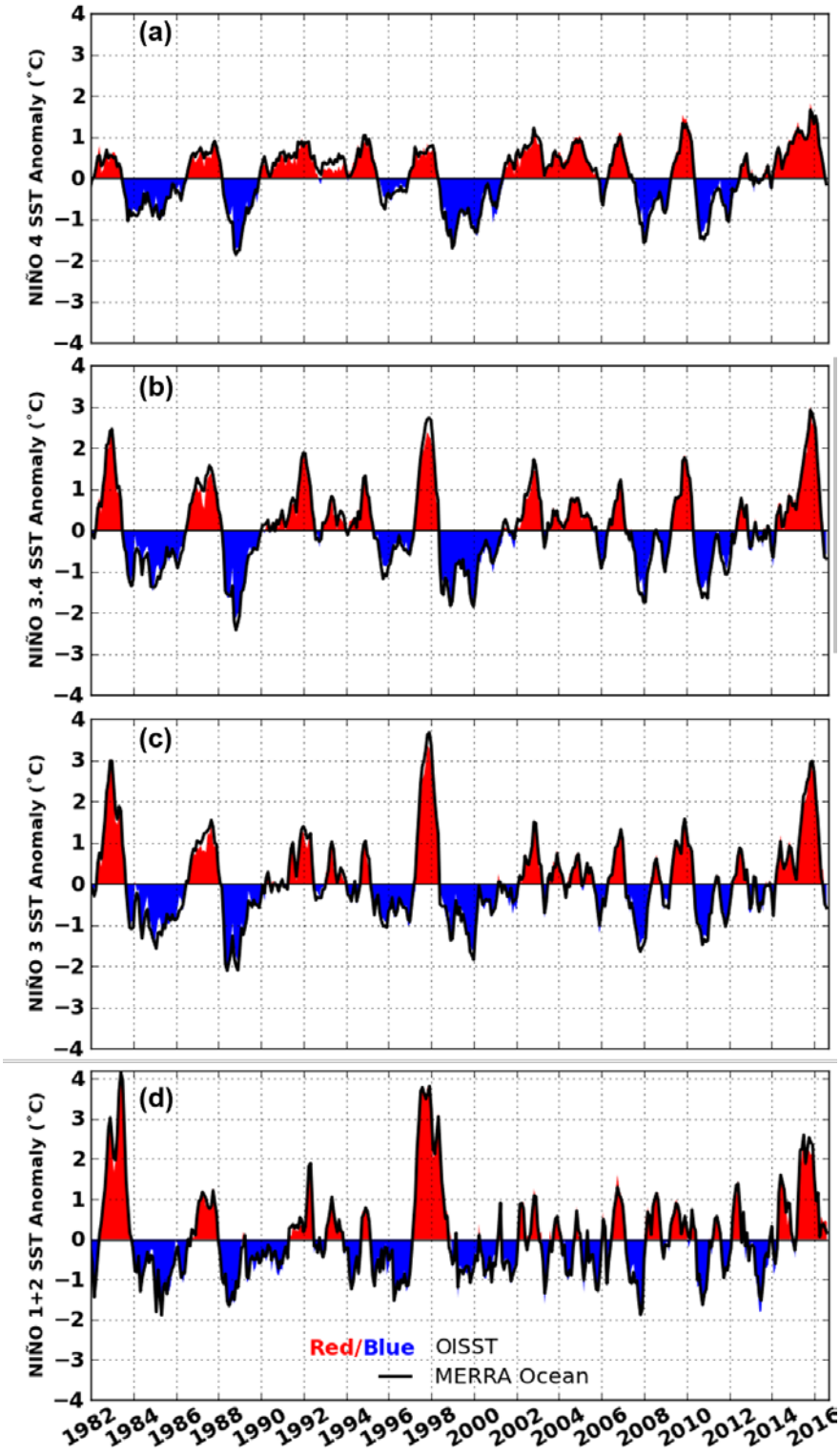

Figure 2. Time series of sea surface temperature (SST) anomaly averaged over a) Niño 4, b) Niño 3.4, c) Niño 3, and d) Niño 1+2 regions for the period 1982–2016. The red/blue shaded curves show the Reynolds OISST while the solid curve represents the analyzed values from GEOS-5 MERRA-Ocean.

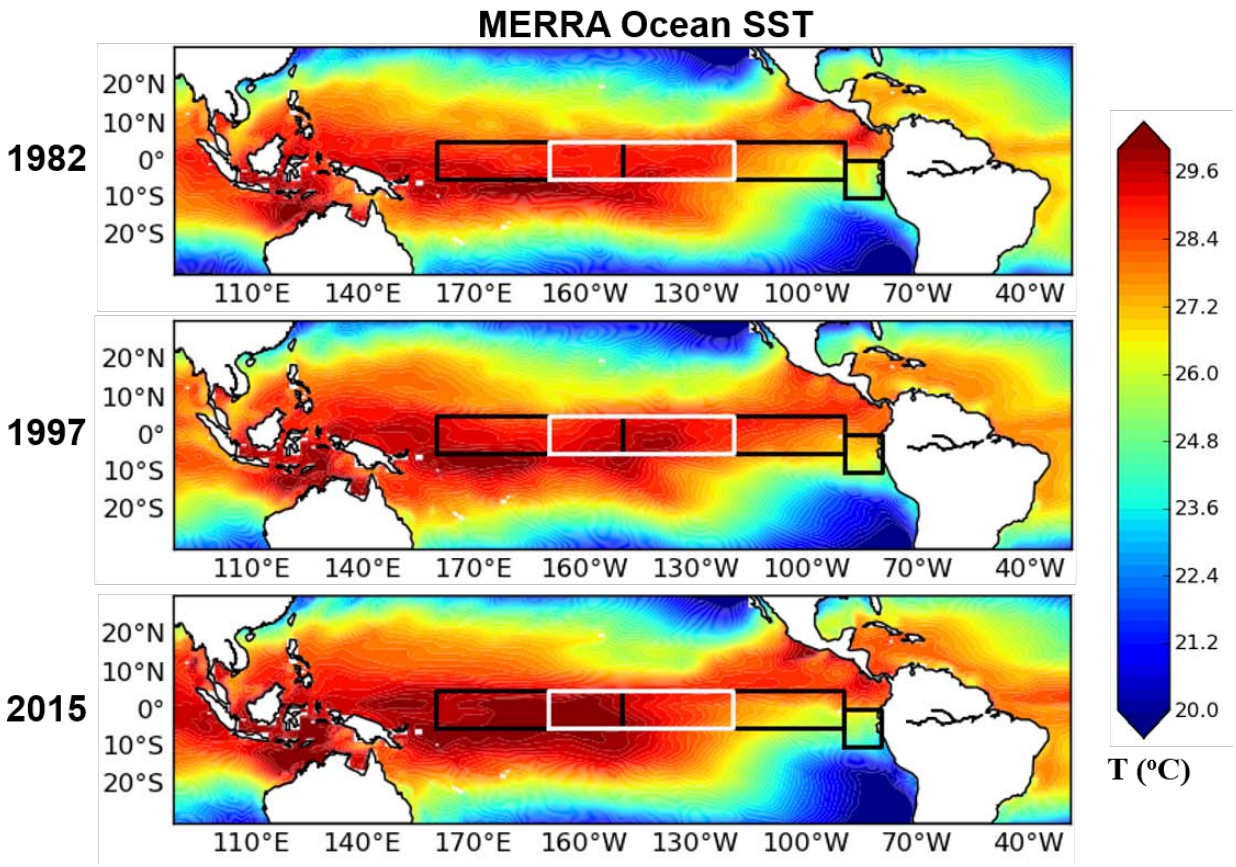

Figure 3. SST over the tropical Pacific from MERRA Ocean for December 1982 (first row), December 1997 (second row) and December 2015 (third row). The highlighted boxes from West to East are Niño4, Niño 3.4 (white), Niño 3, and Niño1+2.

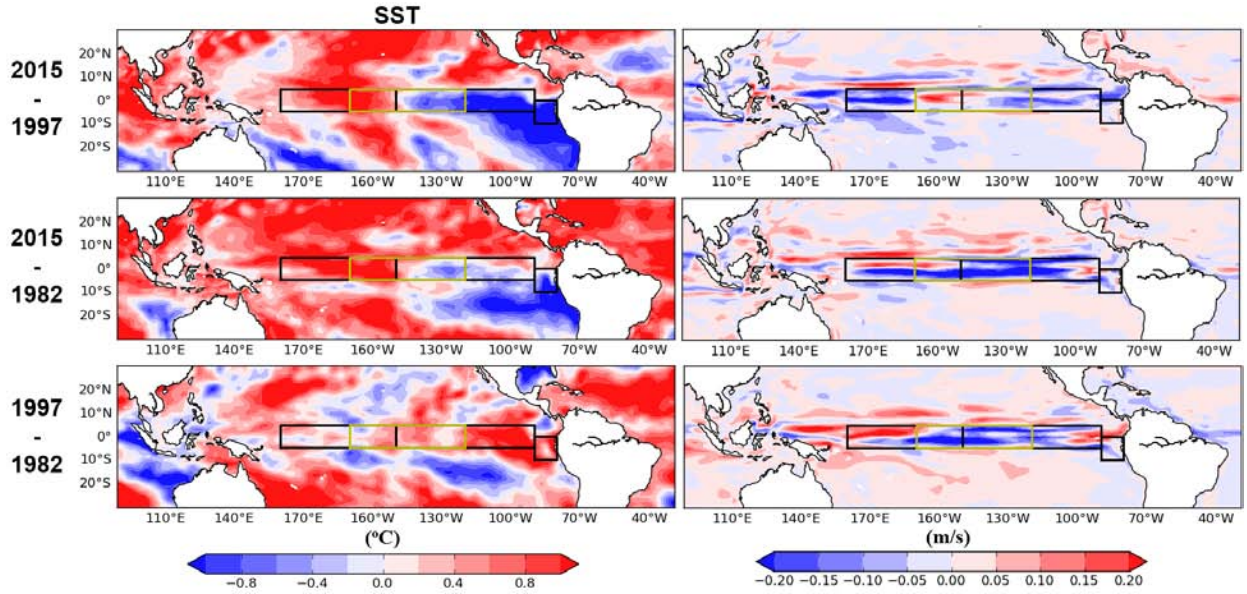

Figure 4. Difference fields over the tropical Pacific from MERRA-Ocean for December 2015 minus 1997 (top row), December 2015 minus 1982 (second row), and December 1997 minus 1982 (bottom row). The difference fields shown are SST (left column) and zonal ocean current velocity (right column). The highlighted boxes from West to East are Niño4, Niño 3.4, Niño 3, and Niño1+2.

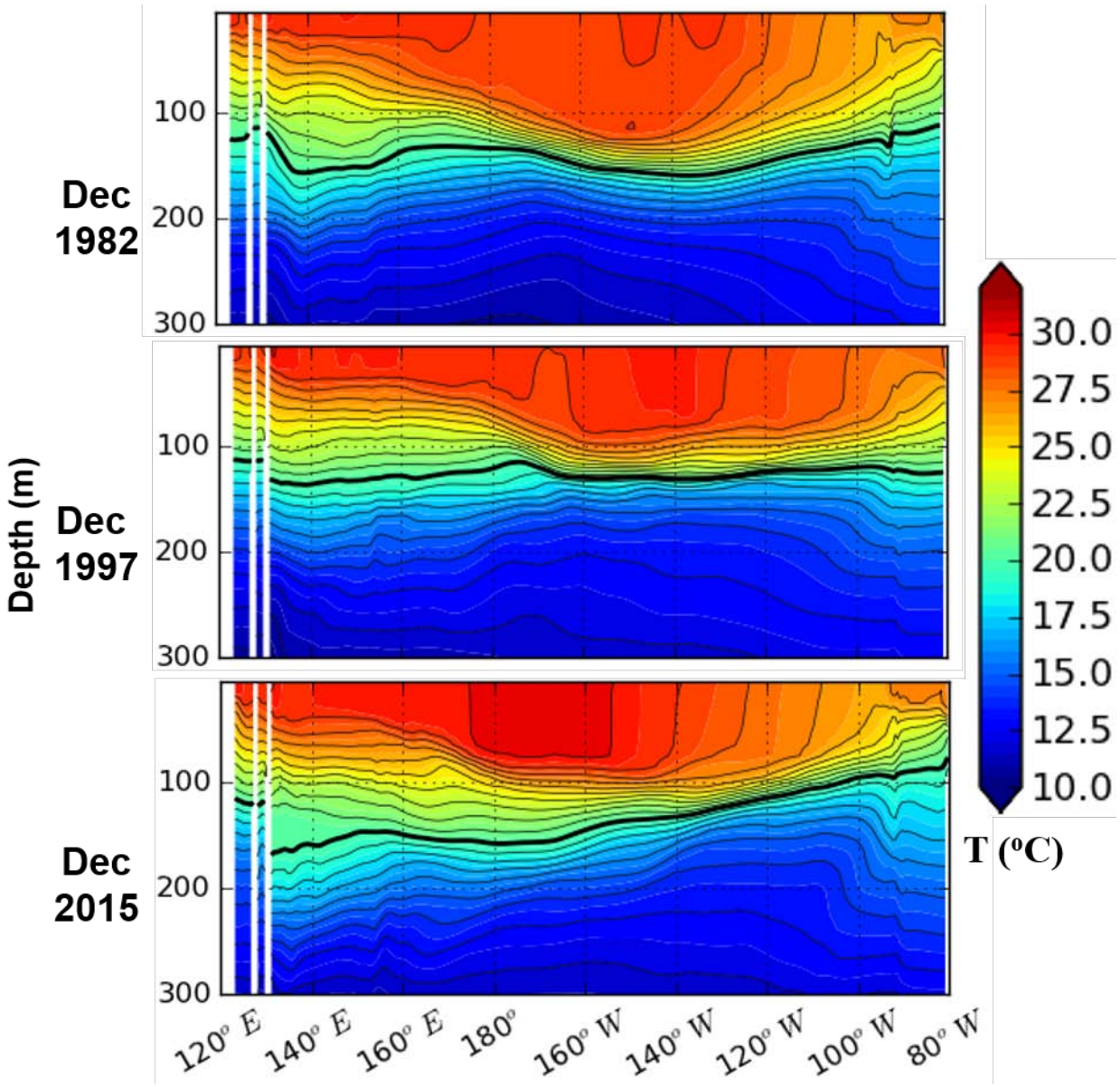

Figure 5. Comparison of longitude-depth sections of sub-surface water temperature (°C) from MERRA-Ocean along the equator during the El Niño mature stage in December of 1982, 1997 and 2015. The bold black line depicts the location of 20°C isotherm.

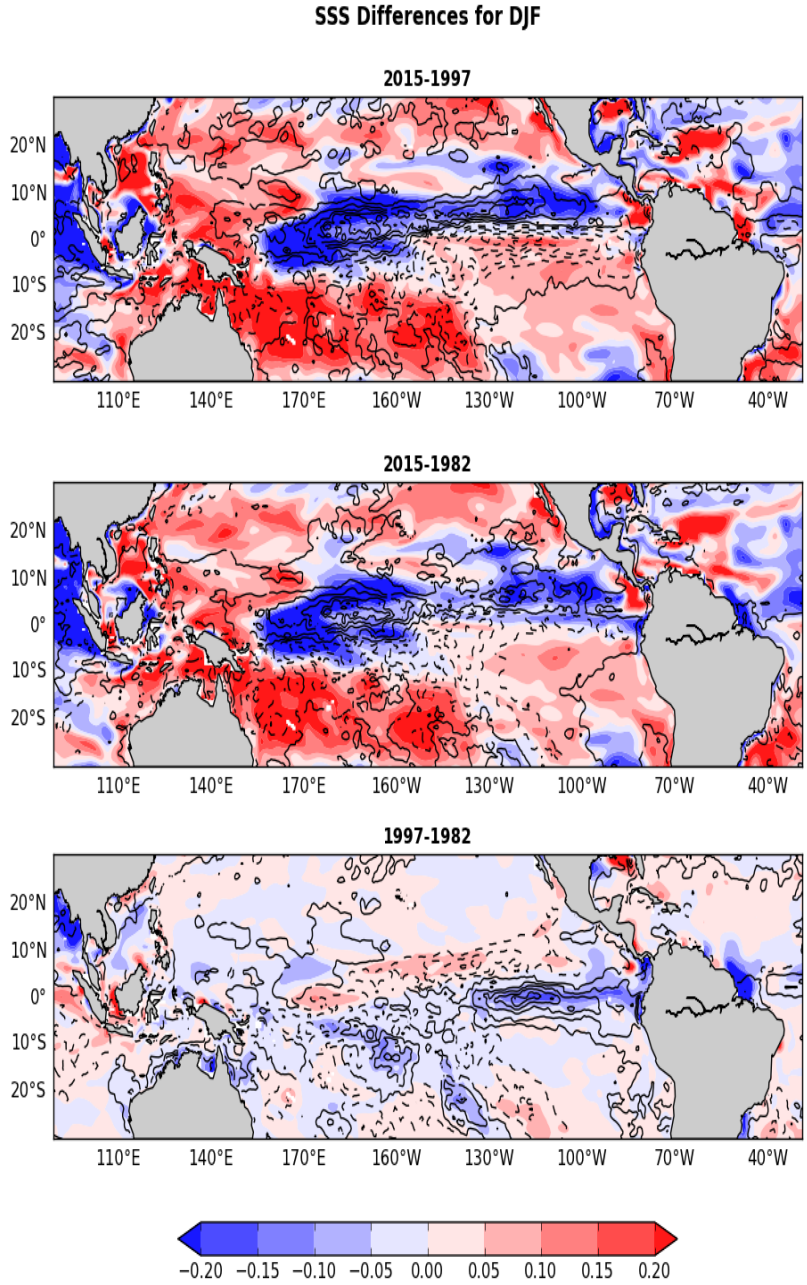

Figure 6. Difference fields in sea surface salinity (SSS) (shaded) over the tropical Pacific from MERRA-Ocean for DJF 2015 minus 1997 (top row), DJF 2015 minus 1982 (second row), and DJF 1997 minus 1982 (bottom row). Contoured is the same as SSS but for precipitation minus evaporation from MERRA-2.

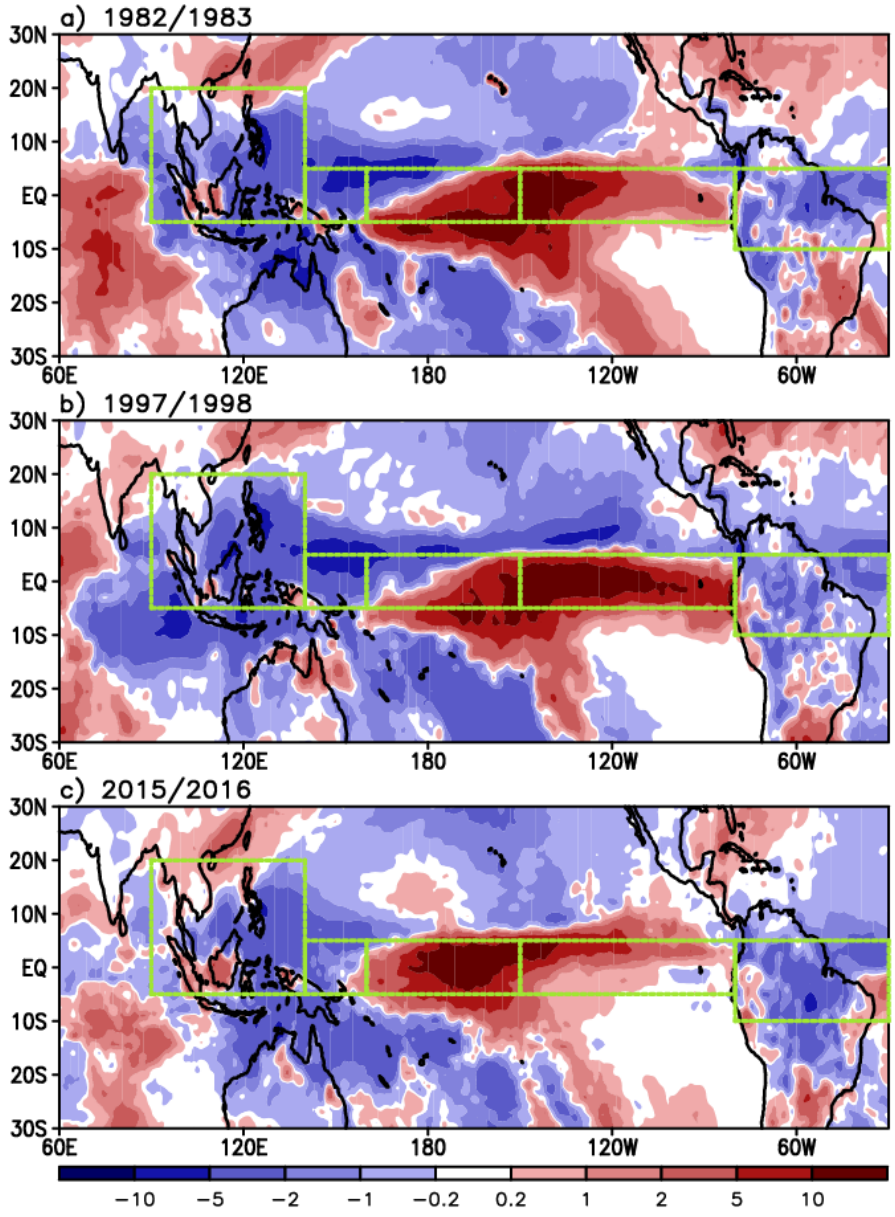

Figure 7. Total precipitation anomalies [mm d^{-1}] in boreal winter (December, January, and February) of the three strongest El Niño years. Dashed boxes denote the areas where area-averaged 2 meter air temperature and precipitation anomalies are calculated (see Table 1).

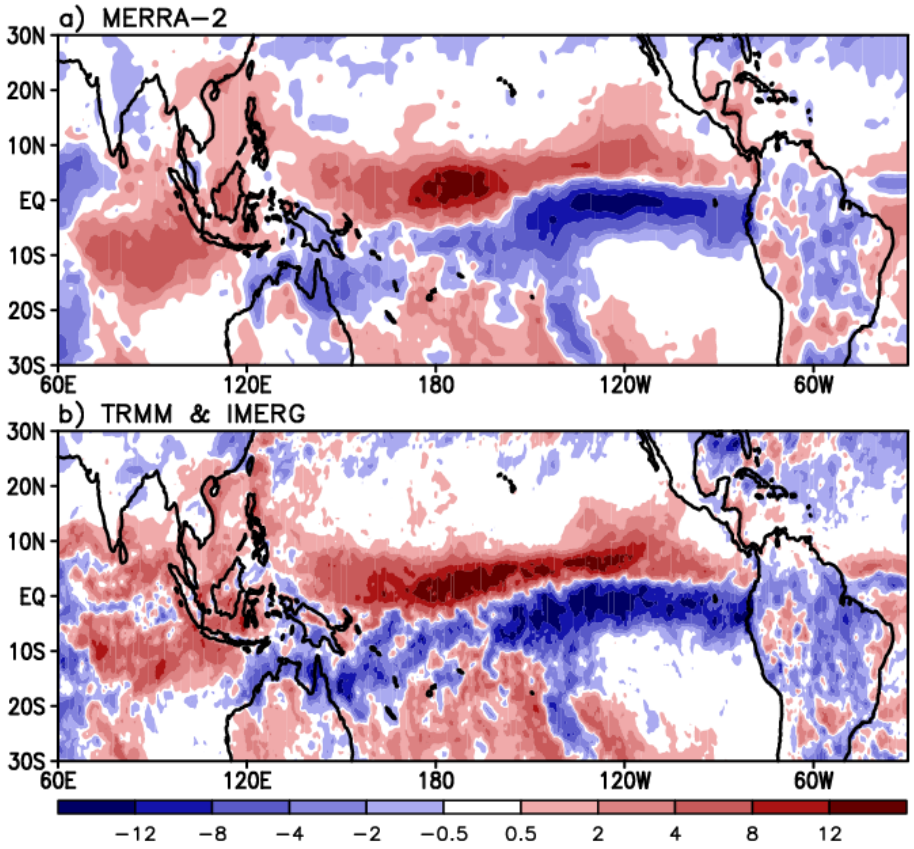

836
837 **Figure 8**: Difference in total precipitation [mm d^{-1}] between 2015/2016 and 1997/1998 El Niño
838 (2015/2016 minus 1997/1998) from MERRA-2 (top panel) and TRMM and IMERG observation
839 (bottom panel).
840

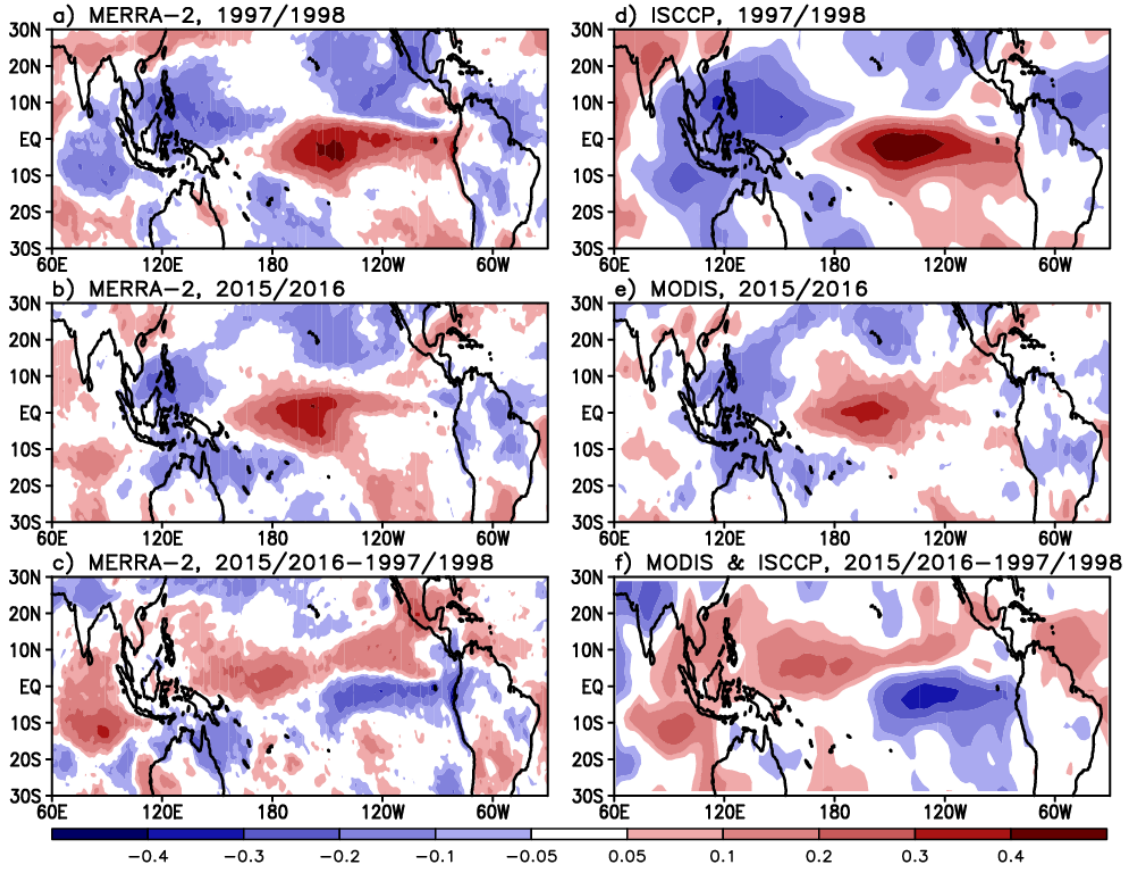

Figure 9: MERRA-2 total cloud fraction anomalies in boreal winter of 1997/1998 and 2015/2016 El Niño events and their comparison with observations from the ISCCP (top panel, 1997/1998 El Niño) and the MODIS (middle panel, 2015/2016 El Niño). The bottom panel represents the difference in total cloud fraction anomaly between the two El Niño events from MERRA-2 (lower-left) and MODIS/ISCCP observation (lower-right).

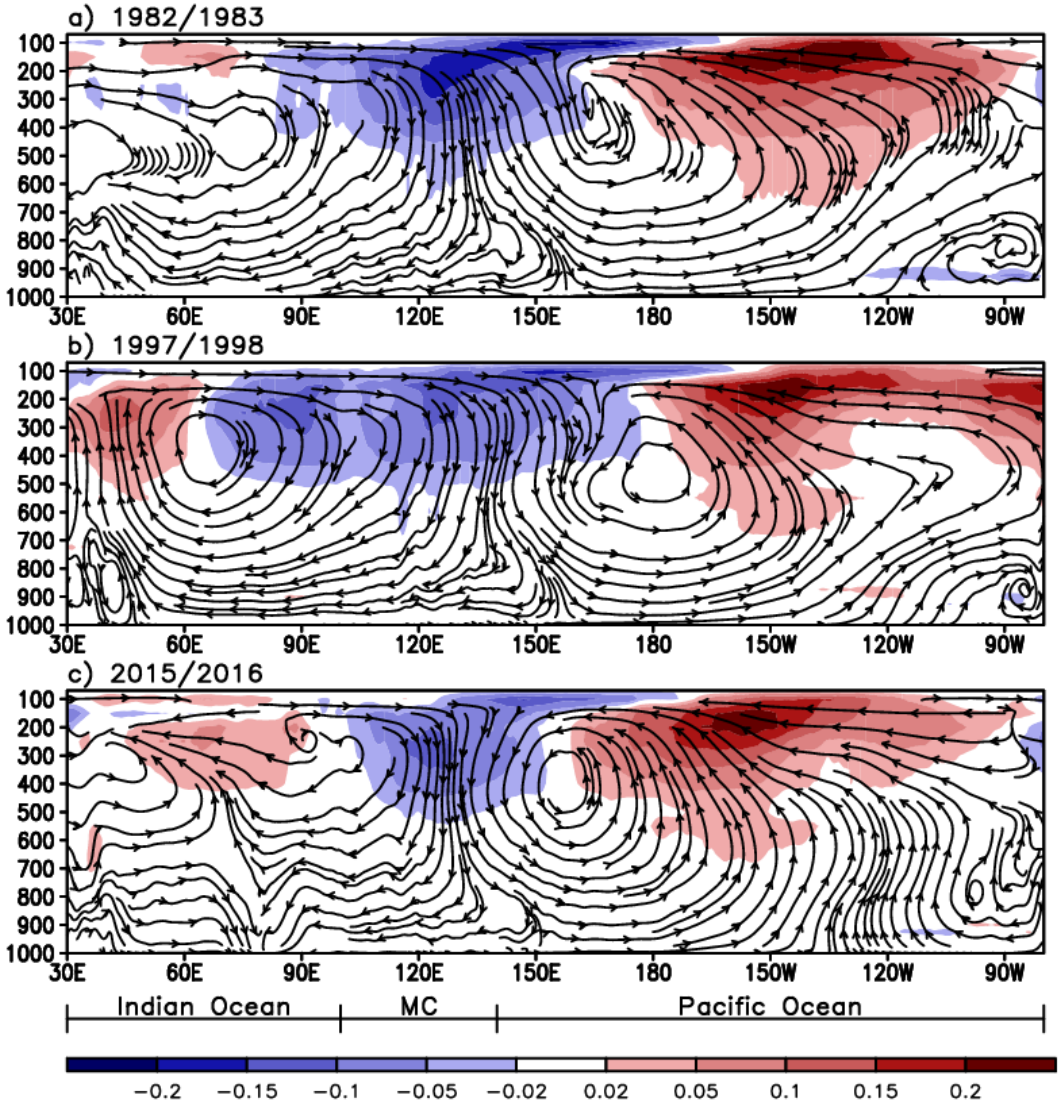

848
849 **Figure 10**. Longitude-pressure [mb] sections along the equator (10°S-10°N averaged) showing
850 the Walker circulation (streamlines) and total cloud fraction anomalies (shaded) over the Indian
851 Ocean, Maritime Continent, and Pacific. The plots are for the boreal winters (December through
852 February) of (a) 1982/1983, (b) 1997/1998, and (c) 2015/2016.
853

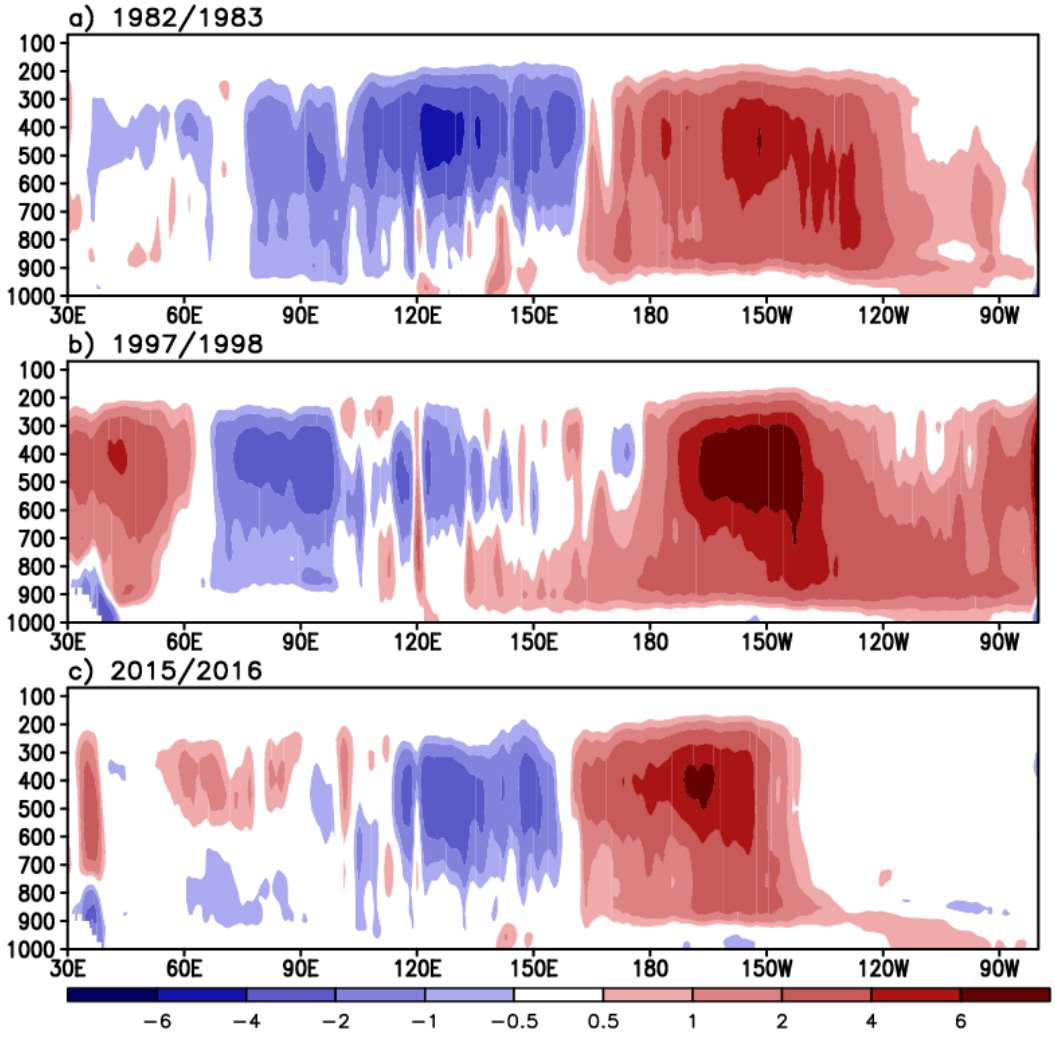

Figure 11. Same as Figure 10 but for the total diabatic temperature tendency [K d^{-1}] anomaly. This value is the outcome of the multiple thermodynamic processes that include moist (e.g., latent heat and convection), radiation, near-surface turbulence (e.g., sensible heat flux), and frictional dissipation of kinetic energy (e.g., gravity wave drag and surface friction). Note that the moist process plays the most substantial role in determining this diabatic temperature tendency over the tropics.

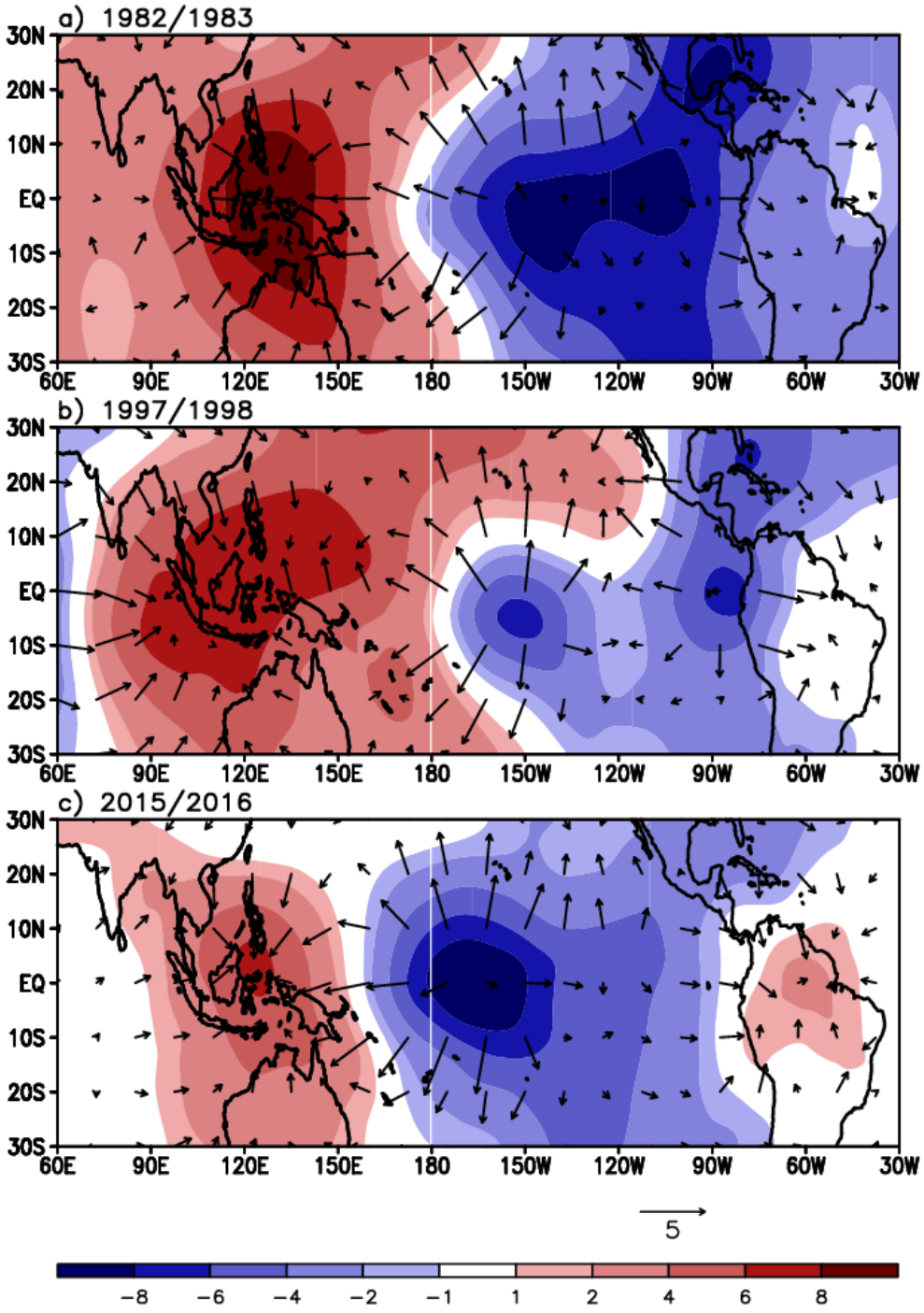

862

863 **Figure 12**. The velocity potential [10^6 m^2s^{-1}] (shaded) and the divergent wind component [m s^{-1}]
864 (vector) in the upper-troposphere (200mb) in the boreal winters of (a) 1982/1983, (b) 1997/1998,
865 and (c) 2015/2016.

866

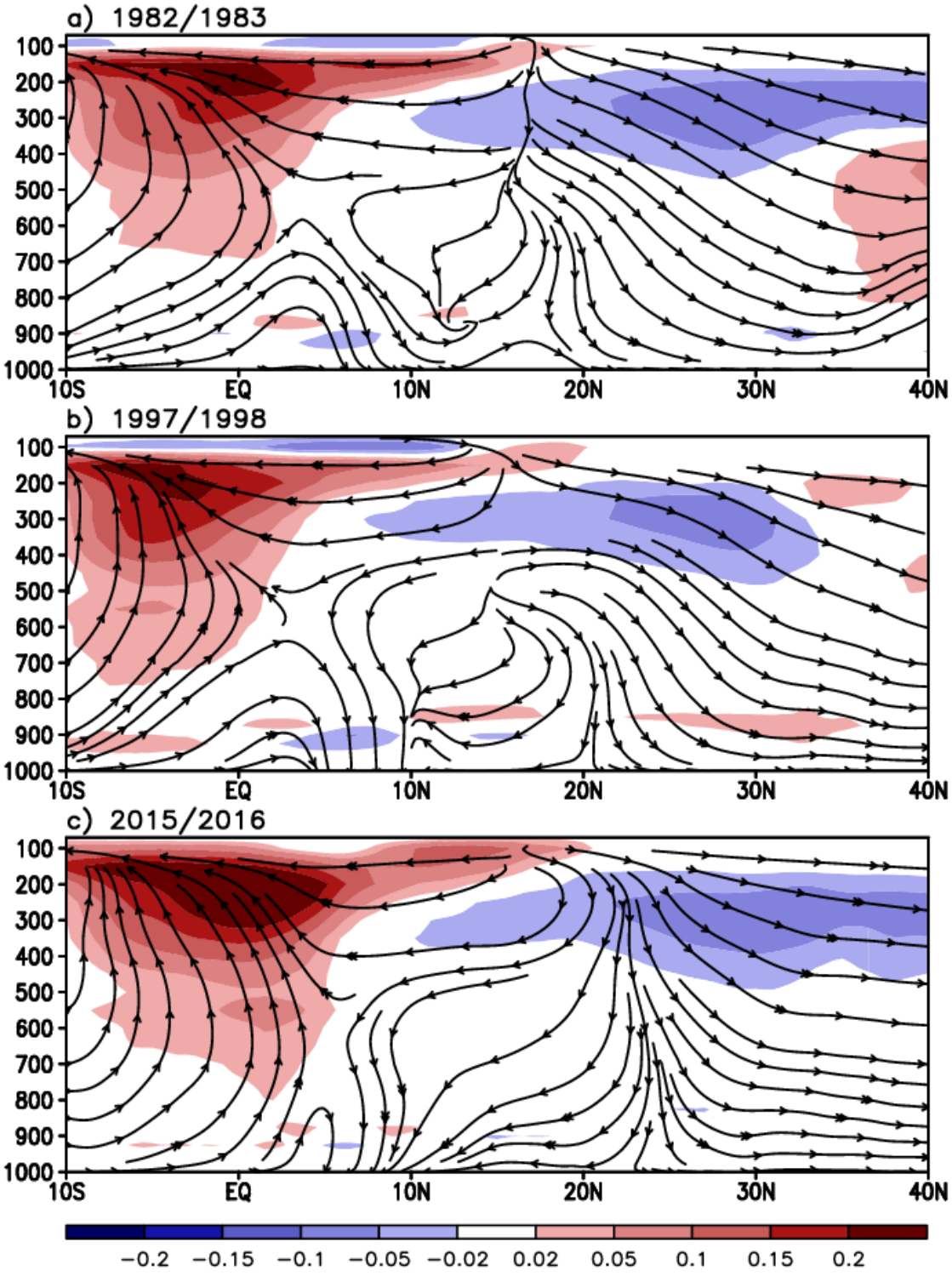

Figure 13. Latitude-pressure sections showing the Hadley circulation (streamline) and total cloud fraction anomalies (shaded), averaged over the longitude range between 150°W and the dateline. Plots are shown for the boreal winters of (a) 1982/1983, (b) 1997/1998, and (c) 2015/2016.

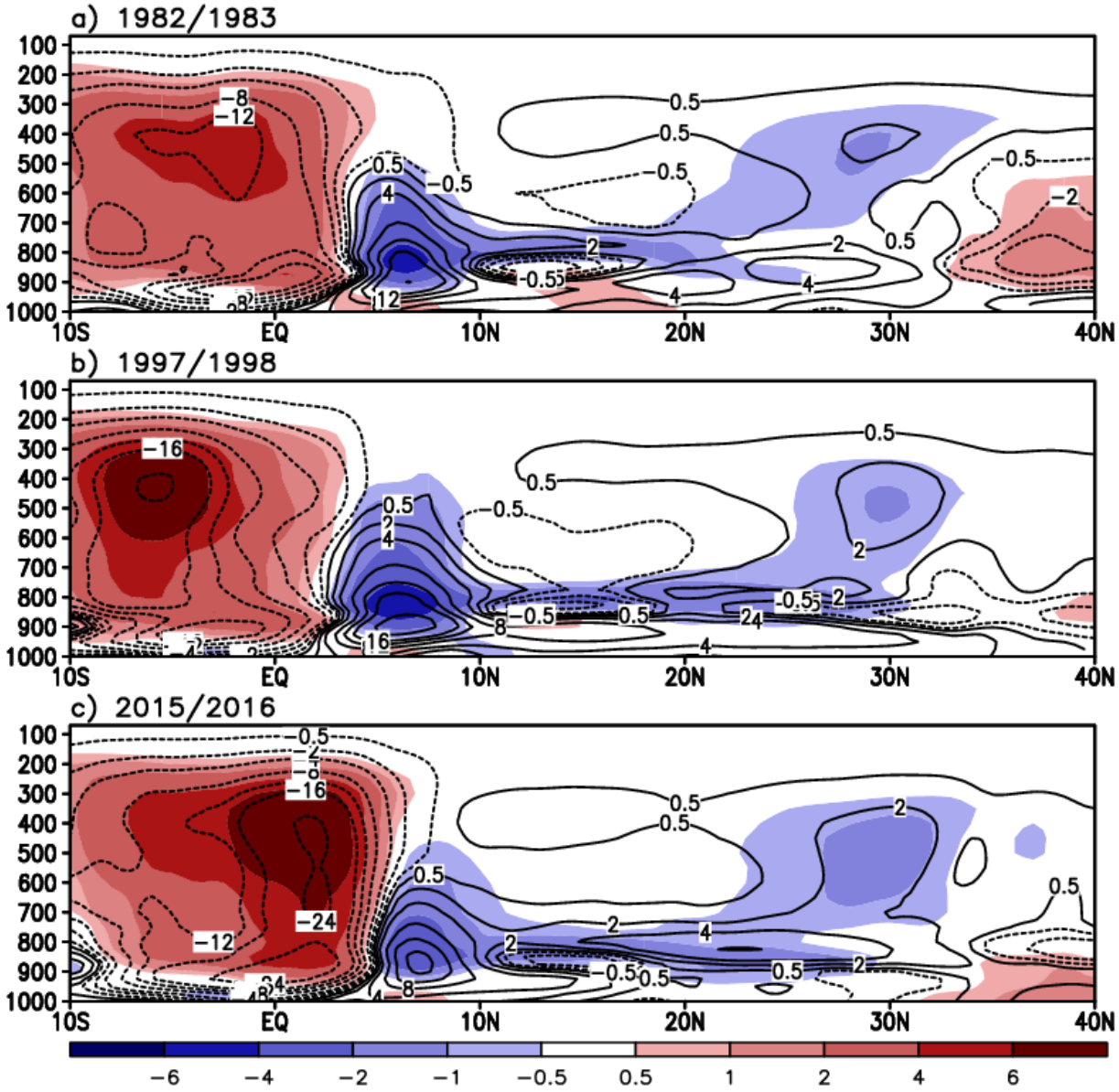

Figure 14. Same as Figure 13 but for the total diabatic temperature tendency [K d^{-1}] (shaded) and specific humidity tendency [10^{-4} kg kg^{-1} d^{-1}] due to moist process (contoured).

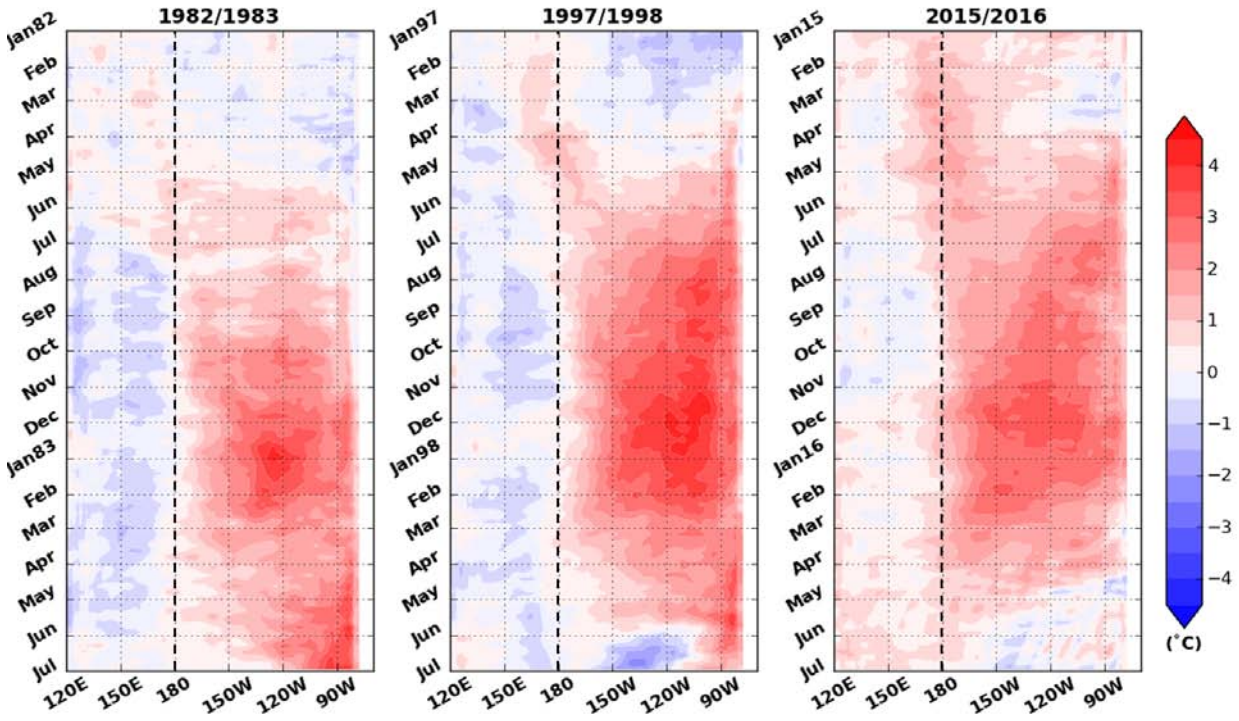

877
878 **Figure 15**. Time evolution of the equatorial Pacific sea surface temperature anomalies (averaged
879 over 5°S–5°N) during the three strongest El Niño years, 1982/1983 (left), 1997/1998 (middle),
880 and 2015/2016 (right). The x-axis represents longitude whereas the y-axis is the time in months.
881

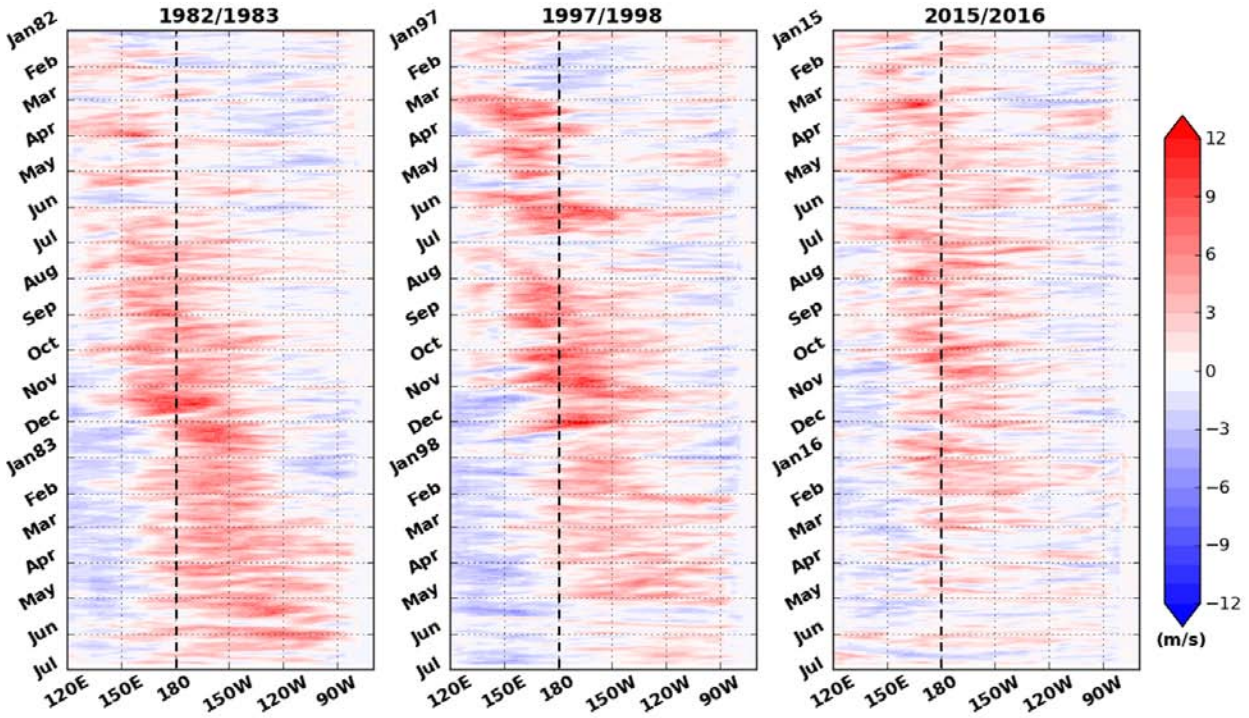

Figure 16. Time evolution of the daily equatorial 10-meter zonal wind anomalies [m s^{-1}] (averaged over 5°S–5°N) during the three strongest El Niño years, 1982/1983 (left), 1997/1998 (middle), and 2015/2016 (right). The x-axis represents longitude whereas the y-axis is the time in months.

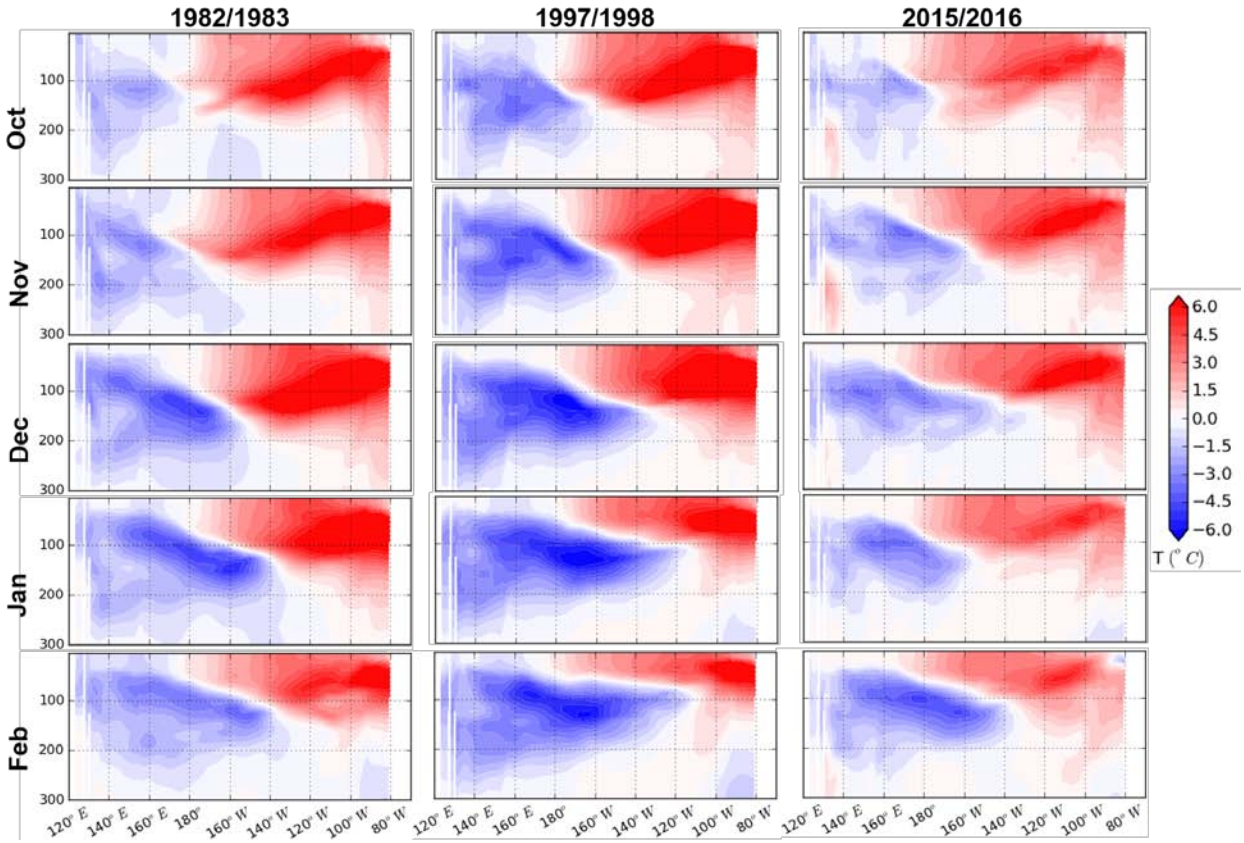

Figure 17. Sub-surface water temperature anomalies [°C] along the equatorial Pacific for the 1982/1983 (left), 1997/1998 (middle), and 2015/2016 (right) ENSO events as the El Niño approaches maturity from October (top) to the beginning of the decay (bottom). The y-axis on the sub-surface water temperature anomaly pattern is the ocean depth in meters.

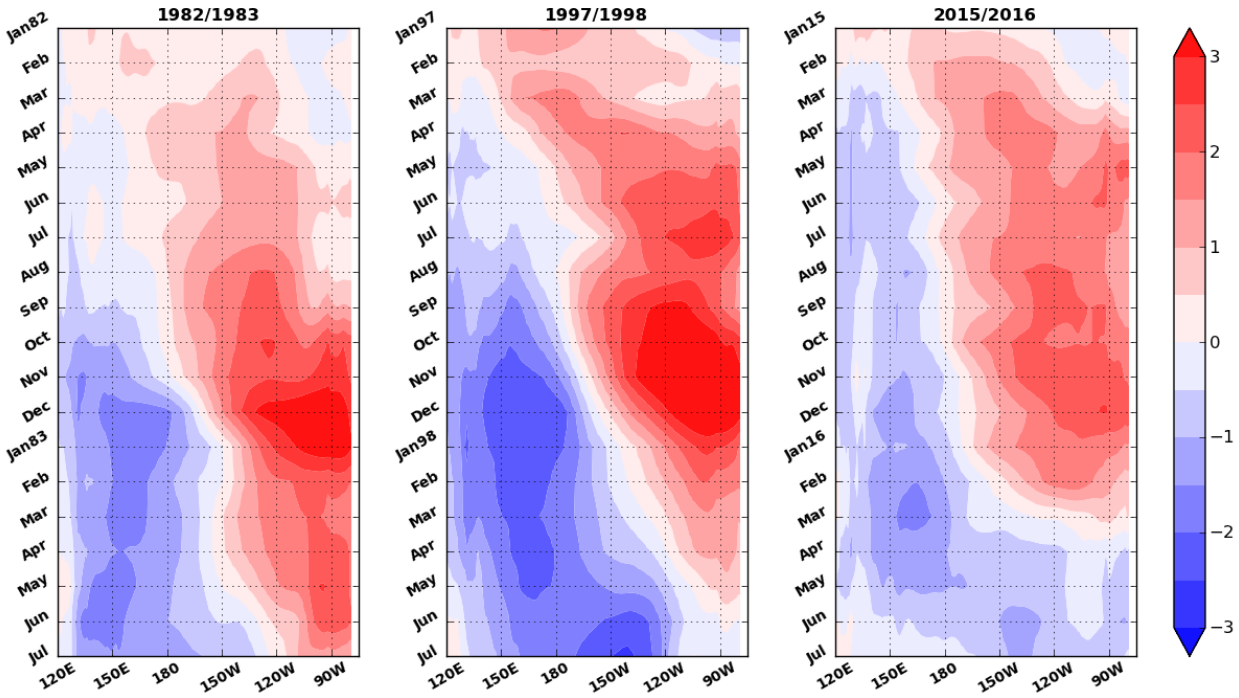

894

895 **Figure 18**. Same as Fig. 15 but for the ocean heat content anomaly

896

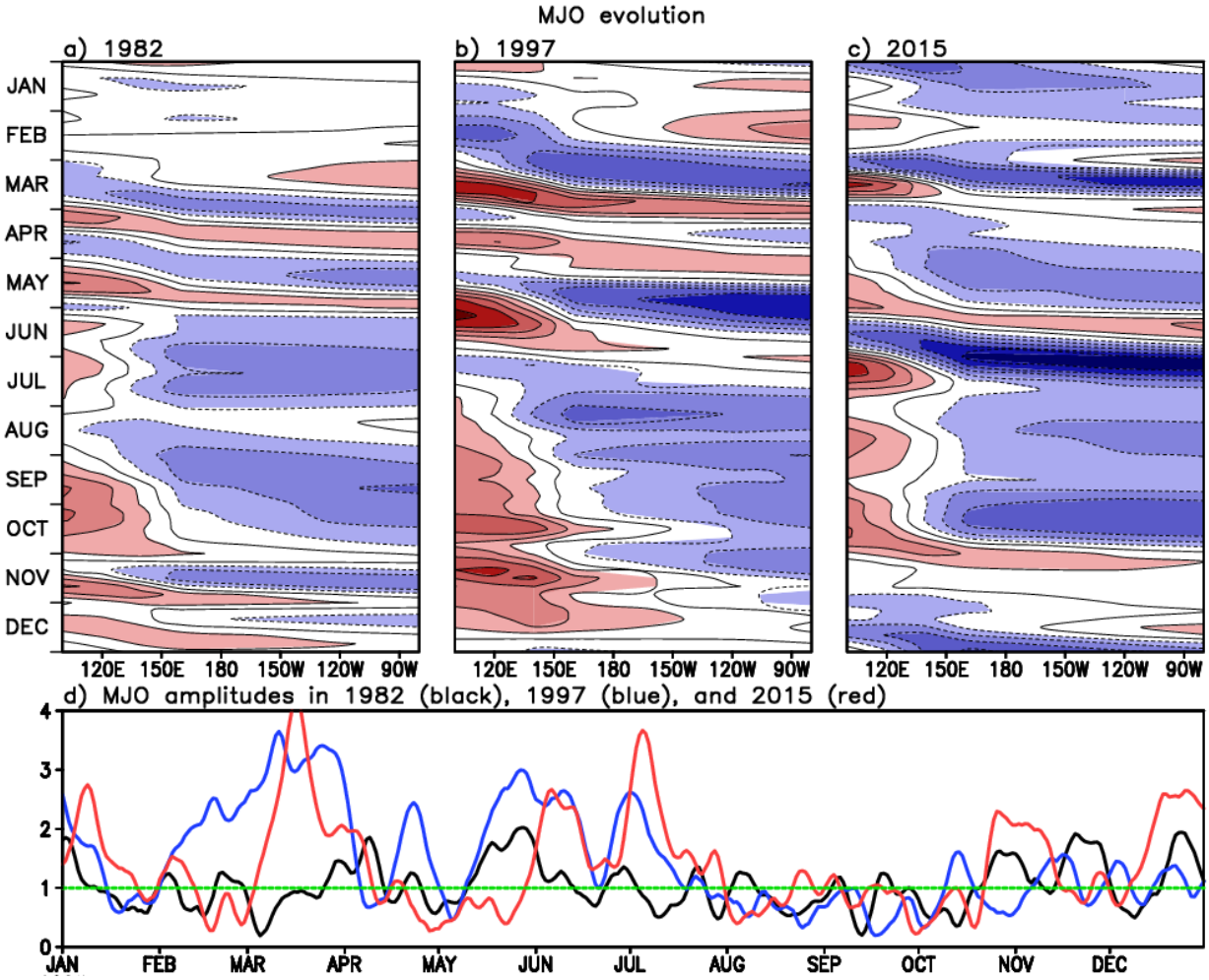

Figure 19. Upper: Time evolution of the MJO propagation along the equatorial Pacific for the period 1982 (left), 1997 (middle), and 2015 (right). The blueish (reddish) color represents the enhanced (suppressed) MJO-related convection. Lower: Time series of the MJO amplitude from the Wheeler and Hendon index. Black, blue, and red curve represents 1982, 1997, and 2015, respectively. The x-axis represents longitude whereas the y-axis is the time in month.

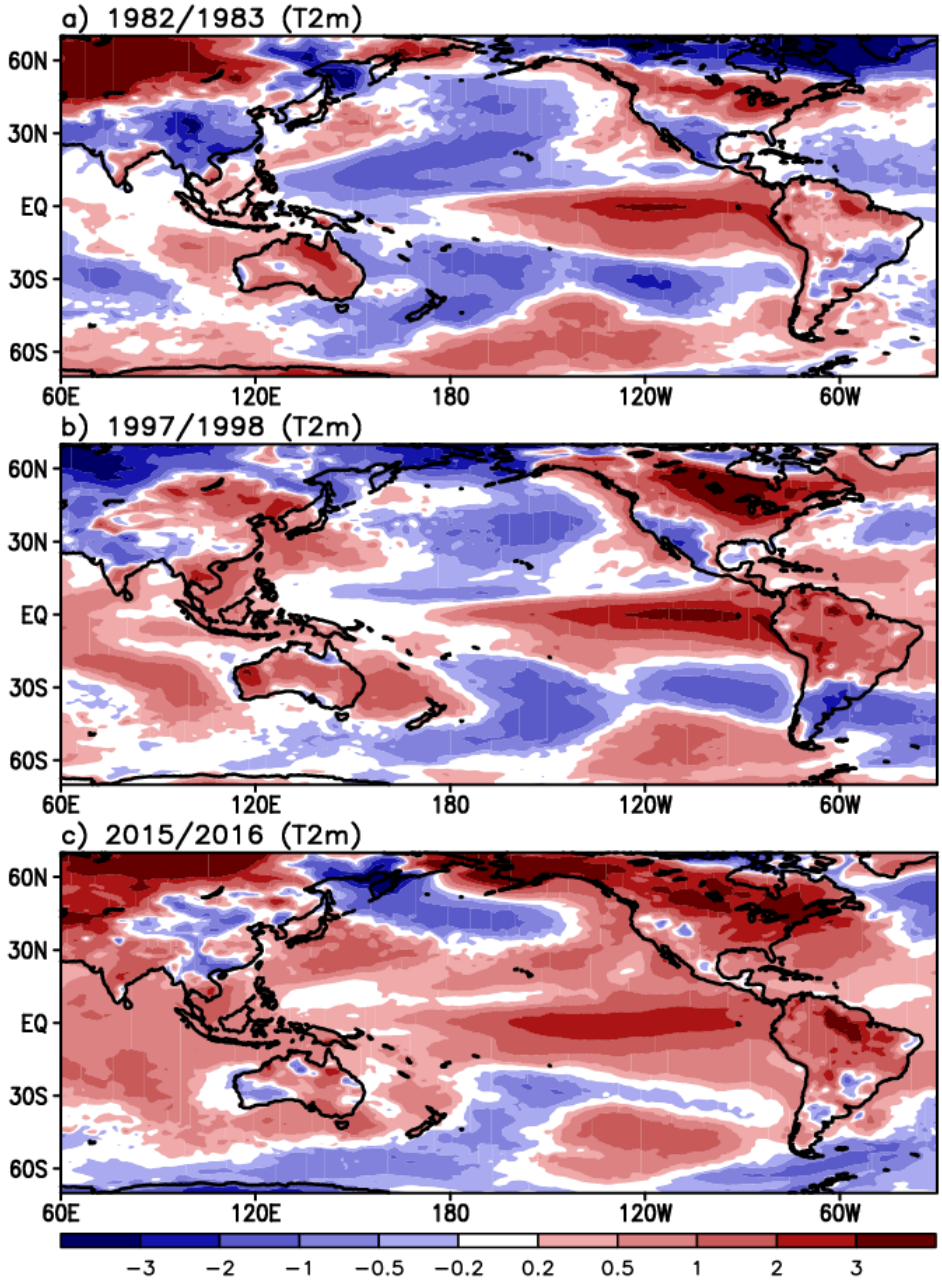

Figure 20. 2 meter air temperature anomalies [°C] in boreal winter (December, January, and February) of the three strongest El Niño years.